A synoptic view of the distribution and connectivity of the mid-crustal low velocity zone beneath Tibet

Yingjie Yang,[1] Michael H. Ritzwoller,[2] Yong Zheng,[3] Weisen Shen,[2] Anatoli L. Levshin,[2] and Zujun Xie[3]

[1] Based on 1–2 years of continuous observations of seismic ambient noise data obtained at more than 600 stations in and around Tibet, Rayleigh wave phase velocity maps are constructed from 10 s to 60 s period. A 3-D Vsv model of the crust and uppermost mantle is derived from these maps. The 3-D model exhibits significant apparently inter-connected low shear velocity features across most of the Tibetan middle crust at depths between 20 and 40 km. These low velocity zones (LVZs) do not conform to surface faults and, significantly, are most prominent near the periphery of Tibet. The observations support the internal deformation model in which strain is dispersed in the deeper crust into broad ductile shear zones, rather than being localized horizontally near the edges of rigid blocks. The prominent LVZs are coincident with strong mid-crustal radial anisotropy in western and central Tibet and probably result at least partially from anisotropic minerals aligned by deformation, which mitigates the need to invoke partial melt to explain the observations. Irrespective of their cause in partial melt or mineral alignment, mid-crustal LVZs reflect deformation and their amplification near the periphery of Tibet provides new information about the mode of deformation across Tibet.

1. Introduction

[2] The Tibetan Plateau results from the convergence between the Indian and Eurasian plates, which has been an ongoing process since the Late Cretaceous to Early Paleocene. The physical processes that have controlled the deformation history of Tibet, particularly the potential localization of deformation either in the vertical or horizontal directions remain subject to debate. Two general models are commonly proposed, although there are finer distinctions between them [e.g., *Searle et al.*, 2011]. The first is the "rigid block" model in which deformation is primarily localized along active faults that bound the blocks [e.g., *Avouac and Tapponnier*, 1993]. (General tectonic features are identified in Figure 1a.) The second is the "internal deformation" model where the medium is treated as a non-rigid continuum in which deformation is spread out within the blocks [e.g., *England and Houseman*, 1986; *England and Molnar*, 1997]. In this model, strain, which is clearly localized near the surface, disperses in the deeper crust into much broader ductile shear zones, in which the lithosphere may deform more or less homogeneously vertically via "vertically coherent deformation" [e.g., *Flesch et al.*, 2005] or may be dominated by more rapid ductile "channel" flow in the middle and/or lower crust [e.g., *Bird*, 1991; *Clark and Royden*, 2000; *Beaumont et al.*, 2004; *Searle et al.*, 2011].

[3] Geophysical evidence can help to discriminate between these competing models [e.g., *Molnar*, 1988; *Klemperer*, 2006]. In particular, it is important to provide constraints on whether Tibet deforms in a way that honors the surface expression of crustal blocks and faults and whether pervasive, interconnected weak layers or channels in the crust are observable. There is a growing list and wide variety of evidence that suggests that the Tibetan crust is warm and presumably ductile, including extensive Cenozoic volcanism [e.g., *Chung et al.*, 2005], low electrical resistivity in the mid- to lower-crust [e.g., *Unsworth et al.*, 2005; *Bai et al.*, 2010], satellite magnetic anomalies consistent with a raised Curie isotherm [*Alsdorf and Nelson*, 1999], and the lack of mid- to lower-crustal earthquakes [e.g., *Chu et al.*, 2009; *Sloan et al.*, 2011]. Previous seismological observations include strong P-to-S conversion bright-spots on active source wide-angle reflection data [*Makovsky and Klemperer*, 1999; *Makovsky et al.*, 1999], strong crustal attenuation [e.g., *Xie*, 2004; *Rai et al.*, 2009; *Levshin et al.*, 2010], crustal low velocity features [e.g., *Kind et al.*, 1996; *Cotte et al.*, 1999; *Rapine et al.*, 2003; *Xu et al.*, 2007; *Caldwell et al.*, 2009; *Guo et al.*, 2009; *Li et al.*, 2009; *Yao*

[1]CCFS, GEMOC ARC National Key Centre, Department of Earth and Planetary Sciences, Macquarie University, Sydney, New South Wales, Australia.
[2]Center for Imaging the Earth's Interior, Department of Physics, University of Colorado Boulder, Boulder, Colorado, USA.
[3]State Key Laboratory of Geodesy and Earth's Dynamics, Institute of Geodesy and Geophysics, Chinese Academy of Sciences, Wuhan, China.
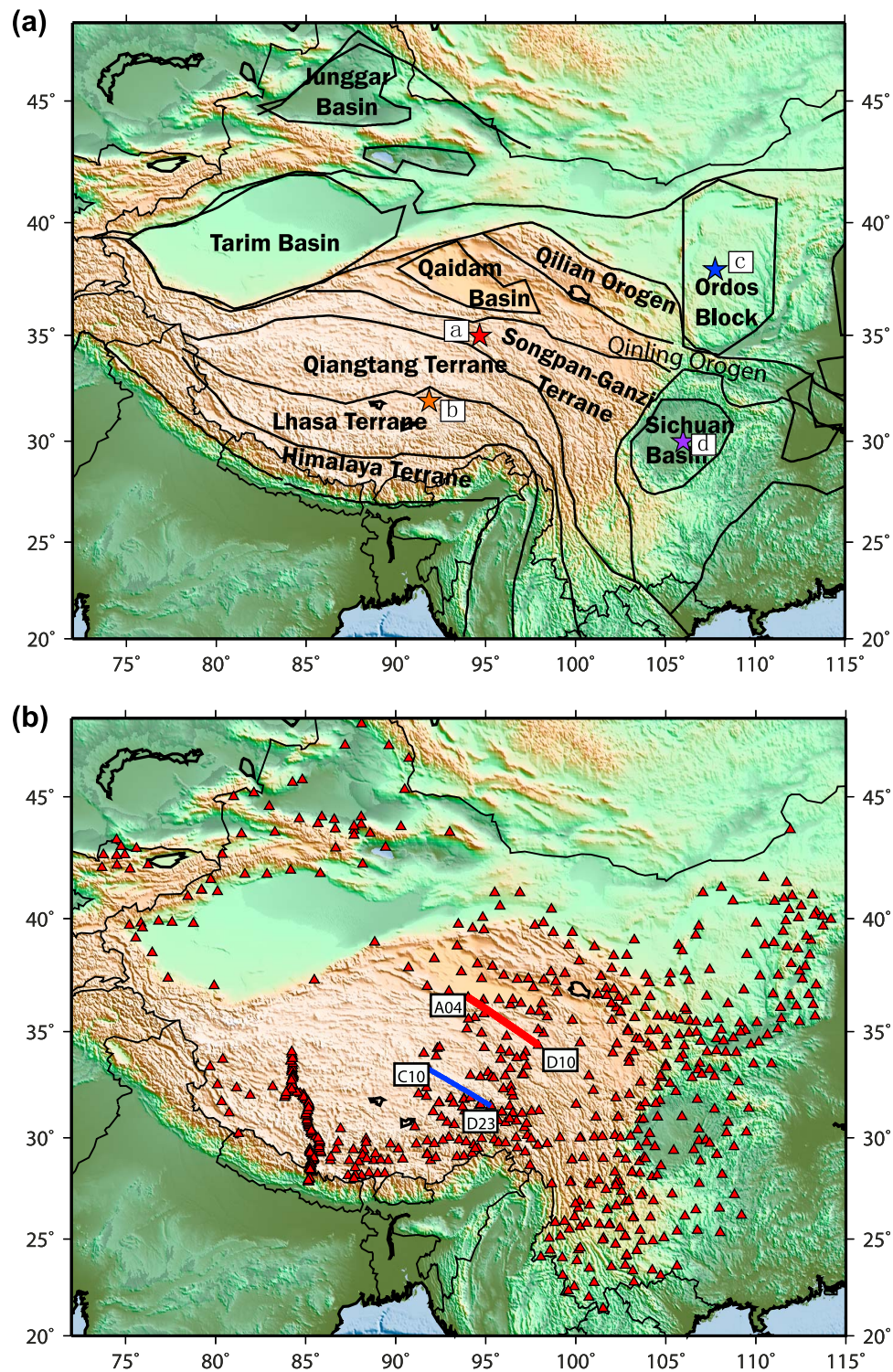
Figure 1. (a) Tectonic and geological regionalization of the Tibetan Plateau. The colored stars denote the locations referred to in Figures 5 and 7. (b) Locations of seismic stations used in this study and the two paths referred to in Figure 3.

et al., 2008, 2010; *Acton et al.*, 2010; *Jiang et al.*, 2011] inferred from receiver functions or surface wave dispersion, and strong radial anisotropy, characteristic of significant shear strains, in the middle crust [e.g., *Shapiro et al.*, 2004; *Duret et al.*, 2010; *Huang et al.*, 2010].

[4] These observations are often taken as prima facie evidence for the existence of partial melt or aqueous fluids in the middle or deep crust beneath Tibet and in some cases for the decoupling or partitioning of strain between the upper crust and uppermost mantle. However, much of this
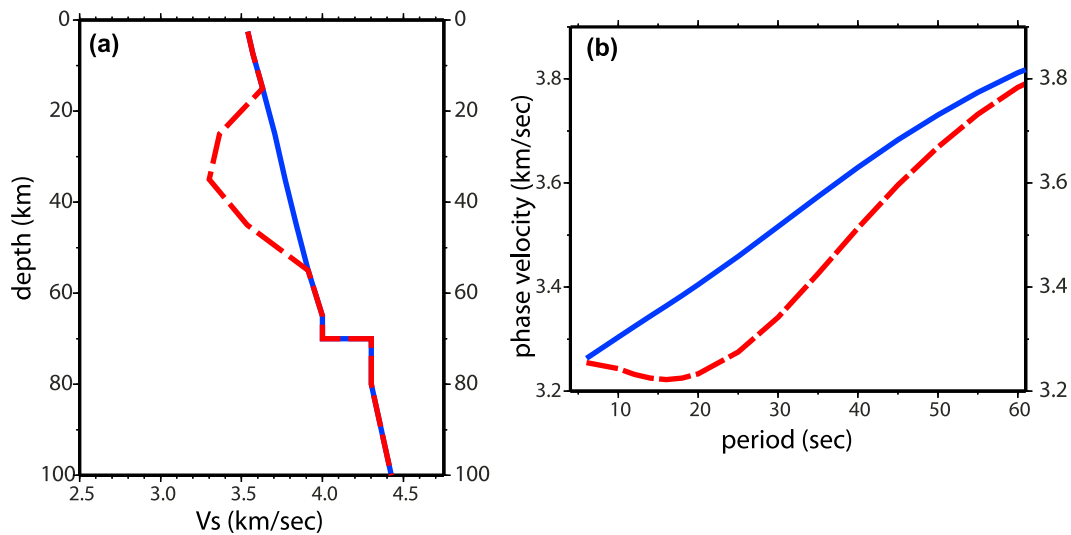
Figure 2. (a) Shear wave speed versus depth for a synthetic model with (red dashed line) and without (solid blue line) a low velocity zone. (b) Dispersion curves computed from the two profiles in Figure 2a, color-coded similarly.

evidence is highly localized along nearly linear seismic or magnetotelluric profiles. This motivates the two questions addressed by this paper: First, how pervasive across Tibet are the phenomena on which inferences of the existence of crustal partial melt rest? In particular, how pervasive are mid-crustal low velocity zones (LVZs) across Tibet? Second, what is the geometry or inter-connectivity of the crustal LVZs observed across Tibet?

[5] We address these questions by producing a new 3-D model of crustal and uppermost mantle shear wave speeds inferred from Rayleigh wave dispersion observed on cross-correlations of long time series of ambient seismic noise. Broad band data from about 600 stations (Chinese Provincial networks, FDSN, PASSCAL experiments), identified in Figure 1b and yielding about 50,000 high quality inter-station dispersion paths, are used to generate Rayleigh wave phase velocity maps from 10 s to 60 s period. The time series in the cross-correlations range from 1 to 2 years in duration. What emerges from this study is a synoptic view of the amplitude, distribution, and inter-connectivity of crustal low velocity zones across Tibet. The principal observation is that significant apparently inter-connected low wave speed anomalies exist across most of the Tibetan middle crust, that these anomalies do not obviously conform to surface faults, and the anomalies are most prominent near the periphery of Tibet.

[6] Figure 2 presents a synthetic example illustrating the dispersion characteristics of a LVZ. Figure 2a shows two synthetic models, one with a well-defined low velocity minimum (red dashed line) and the other without one (solid blue line), and the corresponding synthetic Rayleigh wave phase speed curves are displayed in Figure 2b. A LVZ manifests as very low phase speeds (<3.3 km/s) below 20 s period and, in the absence of near surface sediments, produces a phase velocity minimum between 10 and 20 s period. A change from negative to positive slopes for a Rayleigh wave phase velocity curve can result only from a vertically localized minimum of shear wave speed. Very low Rayleigh wave phase speeds below 20 s period are common

across much of Tibet. For example, Figure 3a displays observed cross-correlations between two pairs of stations for the paths identified in Figure 1b. One of these paths evidences a well-defined minimum in the phase velocity curve (red line in Figure 3b) that must result from a vertically localized minimum in shear velocity. The other curve (blue line in Figure 3b) does not possess the local minimum. However, below 20 s period, the Rayleigh wave phase velocity measured for both paths is very slow, below 3.15 km/s. We will attempt to discriminate between these two types of observations here, although both in principle may be related to partial melt in the middle crust.

[7] The outline of this paper is as follows. In section 2 we summarize the data and tomography that results in Rayleigh wave phase velocity maps from 10 to 60 s period across Tibet. *Yang et al.* [2010] present the primary description of the ambient noise data processing. Evidence for a mid-crustal low velocity zone inferred directly from local dispersion curves is presented in section 3. The construction of the 3D Vsv model and a discussion of its principal features are presented in sections 4 and 5, respectively. In section 6, we discuss the amplitude of the Tibetan mid-crustal low velocity zone as well as its distribution and connectivity. We also consider several corollary questions, including whether the observed mid-crustal low velocity features reflect the existence of partial melt or aqueous fluids, whether they are evidence for vertical decoupling between the crust and uppermost mantle, and whether we observe evidence for lower crustal eclogitization.

2. Data Processing and Tomography

[8] In a related study, *Yang et al.* [2010] applied more or less standard ambient noise tomography [e.g., *Bensen et al.*, 2007; *Moschetti et al.*, 2007; *Yang et al.*, 2007; *Lin et al.*, 2008; *Zheng et al.*, 2008; *Ritzwoller et al.*, 2011; *Zheng et al.*, 2011] to continuous seismic data from about 600 stations in Tibet and surrounding regions recorded during the years 2003–2009 to produce Rayleigh wave phase velocity
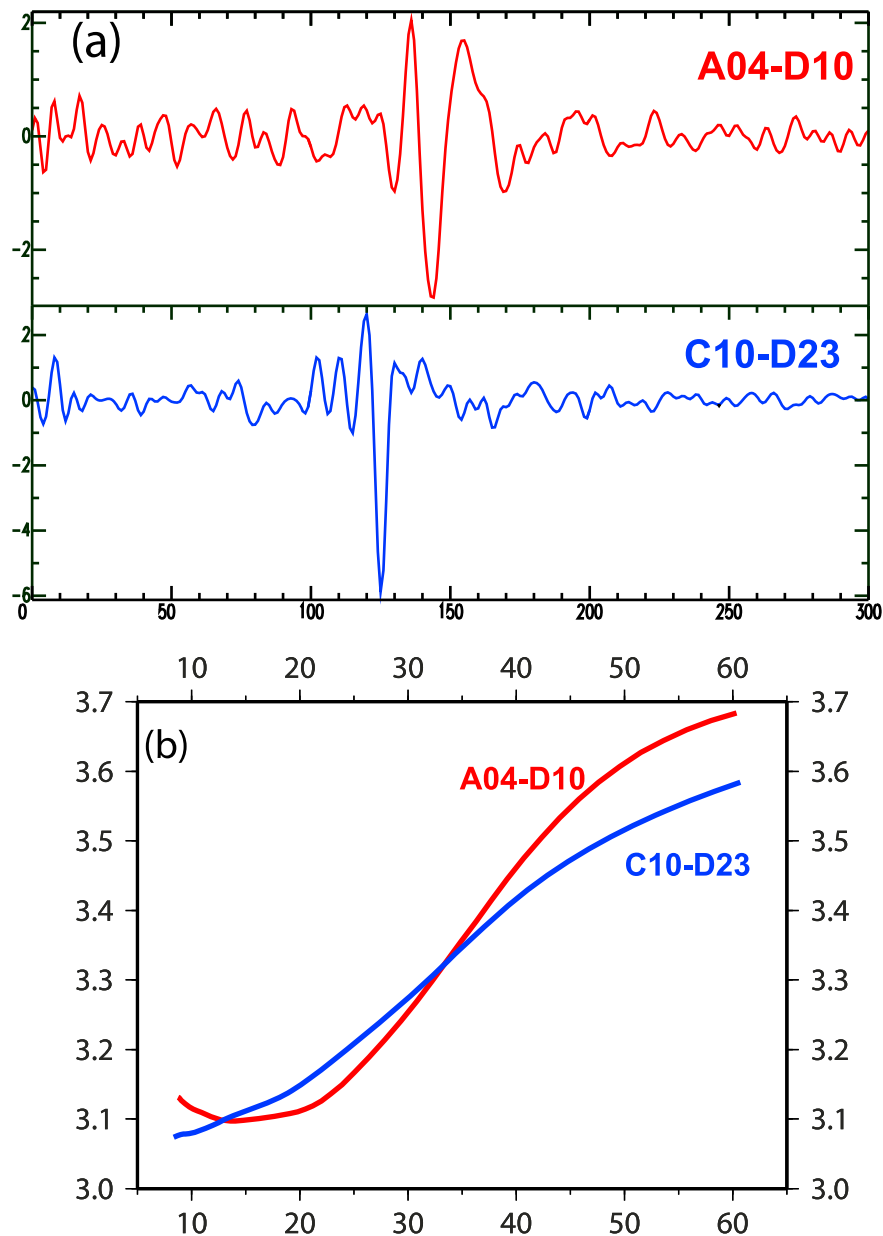
Figure 3. (a) Examples of inter-station cross-correlations of ambient noise observed along the two paths identified in Figure 1b. (b) Rayleigh wave phase velocity dispersion curves computed from the cross-correlations shown in Figure 3a. The stations (A04, D10, C10, D23) are from the ASCENT/INDEPTH IV array. A clear phase velocity minimum is observed on the A04-D10 cross-correlation, which unambiguously indicates a velocity minimum in the crust. The C10-D23 cross-correlation does not show a phase velocity minimum, but exhibits similarly slow phase velocities as the other path.

maps at periods from 10 to 50 s. These stations, shown in Figure 1b, include the permanent Federation of Digital Seismographic Networks (FDSN) across the region, five temporary U.S. PASSCAL experiments in and around Tibet, and Chinese provincial networks surrounding Tibet [*Zheng et al.*, 2009, 2010]. Because different stations are equipped with different types of seismometers, especially among the Chinese stations, instrument responses are removed from continuous seismic data in order to unify the frequency dependent time series recorded at different types of seismometers before performing inter-station cross-correlations.

[9] In removing instrument responses, typically two types of response files may be adopted: Pole/Zero files that represent only the mechanical response of the instruments and RESP files which include digital filtering stages. *Yang et al.* [2010] used Pole/Zero response files because, in principle, both methods should result in the same phase content after removing instrument responses from raw seismograms within the passband of the instrument, which is the case for all the PASSCAL stations in and around Tibet. This was not a good strategy for Chinese stations, however, because when Pole/Zero response files are used more than 90% of the

Figure 4

cross-correlations between Chinese stations display no observable surface waves above 30 s period, whereas most cross-correlations among PASSCAL stations have high signal-noise-ratio surface waves up to 60 s period. Apparently, the Pole/Zero response files of Chinese stations have an problematic cut-off period around 30 s which suppressed the long period (>30 s) signals, even though most of the Chinese stations are installed with broadband seismometers. For this reason, we re-processed all of the Chinese data originally processed by *Yang et al.* [2010], but applied RESP response files to remove instrument responses. This results in observable surface waves at periods longer than 30 s on most cross-correlations among Chinese stations in addition to almost identical surface waves at shorter periods (<30 sec). The phase velocity maps presented here, therefore, are different from those presented by *Yang et al.* [2010] at periods longer than ∼30 s. All details of data processing, quality control, and tomography except for the instrument responses are the same as described by *Yang et al.* [2010], however.

[10] The resulting data set has much better path coverage at periods longer than 30 s and extends up to 60 s. Two examples of phase velocity maps and associated raypath coverage and resolution at periods of 10 s and 40 s are plotted in Figure 4. Resolution at other periods is similar and is estimated to be ∼100–150 km in the region to the east of 90.0°E where station coverage is denser. Resolution degrades to ∼200–300 km in western Tibet where stations are sparser. The new phase velocity maps significantly increase the well resolved area at periods longer than 30 s and also extend the longest period maps to 60 s. This provides better resolution of deeper structures. In regions where the path coverage is good in both the current and previous study, the new phase velocity maps remain nearly identical.

[11] *Yang et al.* [2010] discussed the main features of the phase velocity maps, which we only briefly summarize here. At short periods (e.g., Figure 4a), strong low velocity anomalies are correlated with the major sedimentary basins such as the Tarim, Junggar, Qaidam and Sichuan basins and the northern Ordos Block. At intermediate and long periods (>25 s), e.g., Figure 4b, high velocity anomalies are observed within the Tarim Basin, the Ordos Block and the Sichuan Basin and phase velocities in the Tibetan Plateau are lower than in the surrounding regions, which reflects the thicker crust of the Tibetan Plateau.

3. Local Dispersion Curves

[12] To invert for a 3-D Vsv model from the phase velocity maps, we first extract local phase velocity dispersion curves at each node on a $1° \times 1°$ grid from the phase velocity maps between periods of 10 and 60 s. Most of ambient noise tomography studies performed to date have focused on periods shorter than 40 s because dispersion measurements from cross-correlations of ambient noise data typically have much larger uncertainties at periods above 40 s. In this study, we measure phase velocity dispersion

curves up to 60 s period and evaluate the reliability of the measurements above 40 s period.

[13] One way to evaluate measurement accuracy is to compare tomography maps based on ambient noise data with those based on earthquake data. In southeastern China, *Zhou et al.* [2012] generated phase velocity maps from 6 to 40 s period based on ambient noise data and from 25 to 70 s period based on earthquake data. At the overlapping period of 32 s, they show that the phase velocity maps from ambient noise and earthquake data are similar with a slightly higher average velocity of 0.012 km/s from the earthquake-derived map and with a standard deviation of differences of about 0.038 km/s. The study area of *Zhou et al.* [2012] and this study overlap within E100° to E108° and N26° to N33°, where both studies have good resolution of phase velocities. Within this area, we compare the phase velocity maps at 40–60 s periods from our ambient noise data with those from the earthquake data of *Zhou et al.* [2012]. These two sets of phase velocity maps between 40 and 60 s period are also quite similar to each other, with a standard deviation of differences of about 0.030 km/s and a slightly higher average velocity of 0.01 km/s from earthquake data than from ambient noise data. These results are similar to the comparison at 32 s period by *Zhou et al.* [2012]. The agreement of the phase velocities maps based on ambient noise data and earthquake data encourages us to apply dispersion measurements based on ambient noise data from 40 to 60 s period across the study region.

[14] Examples of local dispersion curves are plotted in Figure 5 for four locations across the region of study, two from Tibet and one each from the Ordos Block and Sichuan Basin. The locations are identified in Figure 1a. The phase velocity curves from the Sichuan Basin and the Ordos Block are quite different from those in Tibet. Much of this difference is due to the thicker Tibetan crust, which lowers phase velocities at periods above ∼25 s. The curves from the Sichuan Basin and the Ordos Block begin to flatten at about 30 s period, which reflects the change of sensitivity from the crust to the upper mantle. This flattening occurs at longer periods for the Tibetan dispersion curves.

[15] We are primarily interested in the more subtle differences in the phase velocity curves within Tibet. On average, the dispersion curves across Tibet at periods longer than 25 s are similar to one another. There are, however, significant geographical variations in the dispersion curves below 25 s period. For example, the dispersion curve (red line in Figure 5) for the Songpan-Ganzi Terrain in northern Tibet has a negative slope between periods of 10 and 20 s, whereas the slope of the dispersion curve is positive for the northern Lhasa terrain in central Tibet (orange line in Figure 5).

[16] As discussed in the Introduction, we take this negative slope between 10 and 20 s period in the phase velocity as clear evidence for a shear velocity minimum in the middle crust. To visualize the spatial distribution of the negative slopes in local dispersion curves, we plot all the slopes of individual local dispersion curves at 11 s period in Figure 6.

Figure 4. (a and b) Rayleigh wave phase speed maps determined from ambient noise at 10 s and 40 s period, presented as the percent perturbation from the average across each map (10 s: 3.05 km/s, 40 s: 3.53 km/s). (c and d) Path coverage of the measured inter-station phase speeds for the overlying maps. (e and f) Resolution of the maps above, presented as twice the standard deviation of the 2-D Gaussian fit to the resolution surface at each point [*Barmin et al.*, 2001].
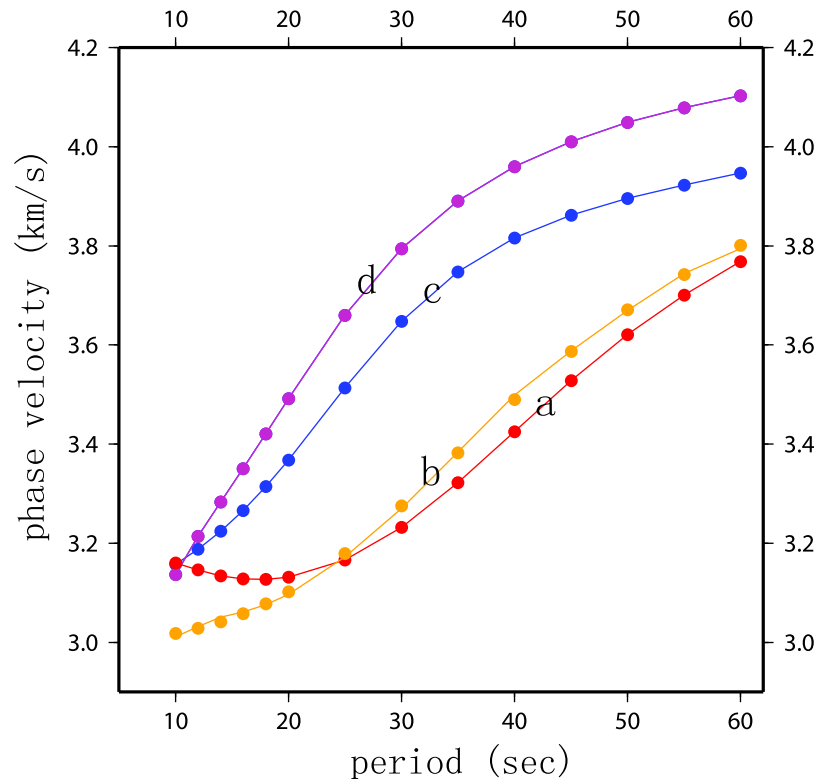
Figure 5. Local Rayleigh wave phase speed curves constructed from the dispersion maps at the four points identified by letters in Figure 1a. The points in Tibet show very slow phase speeds below 20 s period compared with the points in the Sichuan Basin and Ordos Block. Location a is in the Songpan-Ganzi Terrane and displays a phase velocity minimum. Location b, in the northern Lhasa Terrane, has the lowest wave speeds below 20 s period without displaying a phase velocity minimum, demonstrating how sediments can obscure a low velocity zone.

The maps of the slopes of local dispersion curves at other periods up to 16 s are similar. Especially strong positive slopes are observed in the Tarim, Junggar, Qaidam and Sichuan basins as well as in the Ordos Block, indicating that shear velocities increase rapidly with depth. This is reflective both of very low surface velocities due to sediments and the lack of a mid-crustal low velocity zone. Across the Tibetan Plateau, however, the slopes of local dispersion curves are much smaller than the surrounding basin regions. Negative slopes create a ring around the periphery of Tibet, with the strongest negative slopes appearing in northern Tibet. There are also two patches of negative slopes in the western Qilian Orogen and in the Yuan plateau directly to the south of the Sichuan Basin.

[17] From the observation of the distribution of negative slopes on local dispersion curves in Figure 6, we hypothesize the existence of a mid-crustal Vsv low velocity zone in a ring around the periphery of Tibet. Negative slopes in dispersion curves can be obscured, however, by the existence of sediments or amplified by exceptionally high-speed rocks near the surface. To infer the existence, distribution, and amplitude of crustal low velocity zones, therefore, requires the construction of a 3-D Vsv model.

4. Construction of the 3D Vsv Model

[18] We adopt a two-step procedure to construct the 3D Vsv model. The first step is an iterative linearized least squares procedure to estimate a starting model at each point. In the second step, we sample model space around the starting model using a Monte Carlo method to invert each local dispersion curve for a set of 1D Vsv profiles at each node on a $1° \times 1°$ grid. The final 3D Vsv model is then constructed by assembling all of the individual profiles at each location and estimating the mean and standard deviation at each depth. Because only Rayleigh waves are used in the inversion, properly speaking we construct a Vsv model even though we refer to it as a shear velocity model. In the absence of radial anisotropy, Vsv and Vs would be identical, but studies based on single-station earthquake-derived dispersion measurements [e.g., *Ritzwoller and Levshin*, 1998; *Ritzwoller et al.*, 1998] indicate that the middle crust [e.g., *Shapiro et al.*, 2004] and mantle [e.g., *Shapiro and Ritzwoller*, 2002] have strong radial anisotropy across much of Tibet.

[19] Rayleigh wave phase velocities are primarily sensitive to S-wave speeds, less to P wave speeds, and less still to density. We fix density in the inversion and assign the initial density (ρ) from the S-wave model of *Shapiro and Ritzwoller* [2002] using the ρ/Vs ratio of 0.81 [*Christensen and Mooney*, 1995]. We invert only for S-wave speeds but scale P wave to S-wave speed assuming the materials of the crust and uppermost mantle are Poisson solids.

[20] Accurately modeling anelastic effects in the resulting 3-D model is potentially more problematic, particularly because Q of the crustal low velocity zone beneath Tibet
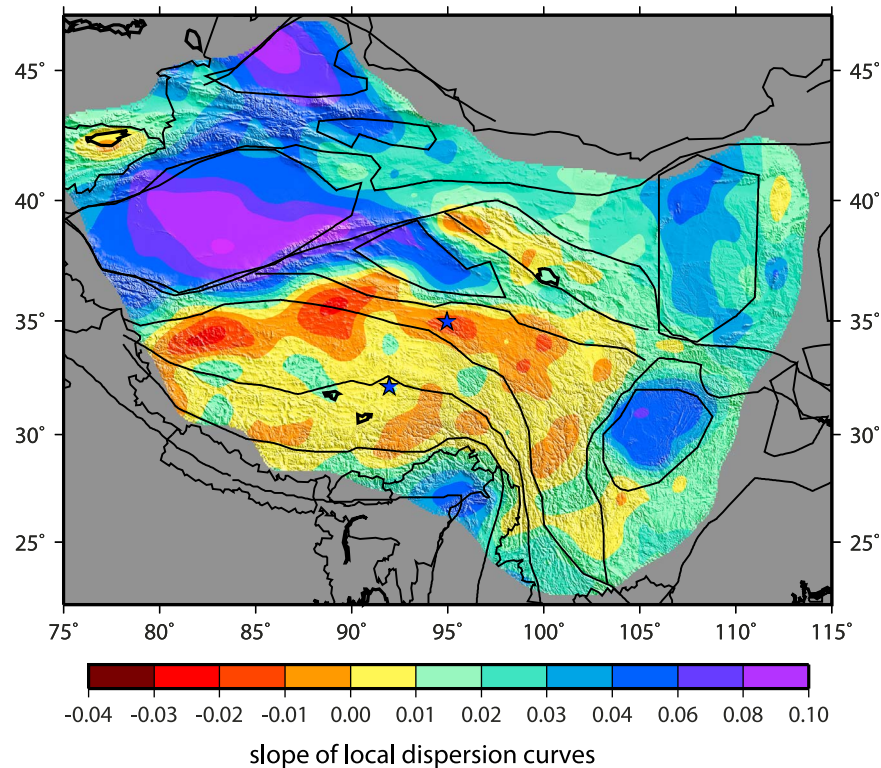
Figure 6. Map of the slope of the local Rayleigh wave dispersion curve at 11 s period. Orange and red colors indicate a negative slope and, therefore, a phase velocity minimum, which is unambiguous evidence of a depth localized velocity minimum in the Tibetan crust.

may be quite low and the amplitude and distribution of crustal Q are largely unknown. In the inversion, we apply a physical dispersion correction [*Kanamori and Anderson*, 1977] using the Q model from PREM [*Dziewonski and Anderson*, 1981], in which shear Q is 600 in the 'lid' (top 120 km), 80 in the uppermost mantle to 220 km depth, and 140 below that. The PREM model is plausible for the Tibetan uppermost mantle, although Q is probably lower in the mantle part of the 'lid' beneath Tibet. Compared to an elastic uppermost mantle, the lower Q of PREM reduces Rayleigh wave phase velocity at 50 s period by about 1%. However, because the Tibetan crust is warm and may possess pockets of partial melt, PREM's crustal Q is much too high and, therefore, the crustal part of the anelastic physical dispersion correction will be underestimated by the PREM Q model. To assess the effect on Rayleigh wave phase velocities of a mid-crustal low Q zone, we computed dispersion curves for the LVZ Vsv model in Figure 2a (red dashed line) using the PREM Q model and compared them to curves from a low crustal Q model in which Q is 80 between 20 and 50 km depth but equal to the PREM Q at other depths. The low crustal Q model reduces Rayleigh wave phase speed relative to the PREM Q model by 5 m/s (∼0.2%) at 10 s period and 17 m/s (∼0.5%) at 20 s period. Because physical dispersion increases with period (although it is offset by decreasing sensitivity to crustal structure), slightly larger physical dispersion effects are seen between 20 s and 30 s period. In this paper we focus on low Rayleigh wave phase velocities between 10 s and 20 s period as diagnostic of low velocities in the middle crust. In this period range, low

crustal Q, which probably accompanies low Vs in the middle crust, will affect Vs by only a small amount (<1%). Therefore, our ignorance of the magnitude and distribution of mid-crustal low Q zones will have a negligible effect on inferences concerning low velocity zones in the Tibetan crust.

[21] In the first step, we perform an iterative linearized least squares inversion. Depth-dependent shear wave speeds are parameterized in eleven constant velocity layers from the surface to a depth of 160 km with layer thickness varying from 5 km at the surface to 50 km near the bottom of the model. Shear wave speeds are fixed to the model of *Shapiro and Ritzwoller* [2002] at depths below 160 km. Predicted phase velocities from the Vsv profiles and their partial derivatives at individual periods with respect to perturbations in Vs at various depths are calculated using the method of Saito DISPER80 [*Saito*, 1988]. During the inversion, shear wave speeds are damped slightly and smoothed vertically between neighboring layers. The predicted phase velocities and partial derivatives are updated iteratively based on refinements in the Vs model. The starting model for the inversion is Vsv from the global model of *Shapiro and Ritzwoller* [2002]. Due to the trade-off between Moho depth and Vs right above and below Moho, strong damping is assigned to perturbations in Moho depth. Thus, the final Moho depths depend strongly on the starting model. Details about the inversion are described by *Yang and Forsyth* [2006] and *Yang et al.* [2008a, 2008b].

[22] In the second step, a Monte-Carlo inversion is performed at each point by taking the results from the linearized inversion as the starting model. The Monte-Carlo method is

similar to the methods presented by *Shapiro and Ritzwoller* [2002] and *Yang et al.* [2008b], but the model space is parameterized using a single sedimentary layer with variable thickness, five cubic B-spline functions for the crystalline crust, and five cubic B-splines for the upper mantle up to a depth of 160 km. Vsv is allowed to vary broadly by perturbing all the B-splines in a range of ± 0.5 km/s and Moho depth is allowed to vary in an interval of ± 5 km, relative to the starting model, i.e., the result of the linearized inversion. In addition, Vsv is constrained to increase monotonically in the crystalline crust in the regions with sedimentary layers but is free to vary in regions without sedimentary layers. This constraint is introduced to reduce model space, in particular the magnitude of the trade-off between the thickness of sedimentary layers and Vs structures at depths directly below the sedimentary layer. The Monte-Carlo inversion searches model space guided by a Metropolis algorithm [e.g., *Mosegaard and Tarantola*, 1995] to generate numerous Vsv models. Only those models that fit the Rayleigh wave dispersion curves with a reduced misfit x^2 less than 1.5 times the minimum misfit x^2_{min} are retained to form the ensemble of "accepted" models. The reduced x^2 misfit is defined as $\chi^2 = N^{-1} \sum_{i=1}^{N} (d_i - p_i)^2/\sigma_i^2$, where N is the total number of discrete dispersion measurements along the phase velocity curve, d_i is one of the measurements with uncertainty σ_i and p_i is one of the predicted dispersion speeds.

[23] Determining the accepted models in the Monte-Carlo inversion requires errors bars for the dispersion curves, which is problematic. We apply the tomographic method of *Barmin et al.* [2001] to obtain the phase velocity dispersion maps and derive the curves from the maps, but this method does not produce local error estimates, only estimates of resolution (Figures 4e and 4f). Reliable error bars can be estimated using Eikonal tomography [*Lin et al.*, 2009], but the uneven station distributions renders this method impossible over the vast majority of the study region. There are, however, two sub-regions where Eikonal tomography does yield meaningful uncertainty estimates: a southeastern area including the Sichuan Basin and the Yunnan plateau and another in central Tibet between E90° and E96° where station coverage is sufficiently dense. Based on the Eikonal tomography results in the two sub-regions, we compute the average uncertainties for local phase velocities, which are about 10 m/s at periods shorter than 30 s but increase to 12.5 m/s at 35 s period and further to 15 m/s at 40 s period. Because the number of measurements decreases toward longer periods, we are not able to perform Eikonal tomography at periods longer than 40 s. Rather, we linearly extrapolate the uncertainties from 40 to 60 s period based on the trend of average uncertainties from 30 s to 40 s. This results in an uncertainty of 22.5 m/s at 60 s period. This is the size of the error bars seen in Figures 7a and 7b. East of E90°, we use these average uncertainties for each grid node because the path coverage and the resolution are quite similar across the entire eastern region. However, west of E90°, where path coverage and resolution degrade, we increase the average uncertainties by 50%. We acknowledge that uncertainties estimated in this way are not ideal, but based on experience gained in the western U.S. and eastern China we believe that they are realistic. Period independent changes to uncertainties in phase velocities will not change the final

model, but will affect the uncertainty level of the resulting 3D Vs model.

[24] Example results of inversion of the two Tibetan local dispersion curves shown in Figure 5 for 1D Vs models are presented in Figure 7. The locations of the dispersion curves are identified with red stars in Figure 1a in the Songpan-Ganzi Terrane (95°E, 35°N) and the northern Lhasa Terrane (92°E, 32°N). The observed local dispersion curves themselves are presented with error bars in Figures 7a and 7b. The ensemble of accepted Vsv models from the Monte-Carlos inversion is plotted in Figures 7c and 7d as a gray corridor, which represents one standard deviation of the Vs model assemblage around the mean. The two blue lines present the corridor for two standard deviations. The predicted phase velocity curves from the models contained in the gray corridor are plotted as gray lines in Figures 7a and 7b.

[25] As expected, due to the negative slope in the dispersion curve seen in Figure 7a, all the members of the ensemble of Vs model at the Songpan-Ganzi location display a low velocity zone (LVZ) with a pronounced velocity minimum. The LVZ extends from about 15 km to 45 km depth with the minimum velocity near 30 km. Any vertically monotonically increasing Vs model at this point cannot fit the dispersion curves within the specified uncertainty, especially in the negative-slope period range from 10 to 20 s. In contrast, at the northern Lhasa location, all Vs profiles increase nearly monotonically with depth without a pronounced shear velocity minimum. Again, this is consistent with the monotonic increase in phase velocities evident in Figure 7b. Although the two model points in Tibet differ with respect to the presence of a shear velocity minimum in the crust, they agree in that shear wave speeds are exceptionally low (<3.3 km/s) between depths of 20 and 40 km.

[26] For each grid point, the mean of the resulting ensemble of acceptable models (bold black lines in Figures 7c and 7d) at each depth is taken as the expected value of the Vs-model and the standard deviation about the mean provides the estimate of model uncertainty. By assembling all the 1-D Vs models for each grid point, we form the 3-D model.

[27] Note that wave speeds in the lower crust trade-off with those in the uppermost mantle. This appears in Figures 7c and 7d as an increase in the width of the ensemble of accepted models near Moho. In addition, the use of B-splines in the crust imposes a strong vertical smoothness constraint, which militates against high velocities in the lowermost crust. Because of these issues we will underplay interpretation of the lower crust in our model. Joint inversion of receiver functions with surface wave dispersion would help to improve estimates of Moho depth as well as shear wave speeds directly above/below the Moho (e.g., W. Shen et al., Joint inversion of surface wave dispersion and receiver functions: A Monte-Carlo approach, manuscript in preparation, 2012) and would help to improve the model in the lowermost crust.

5. The 3-D Vsv Model

[28] Before discussing the geometry, extent, and apparent connectivity of the mid-crustal low velocity zone, we discuss the 3-D model more generally in this section. In order for

(95°, 35°)　　　　　　　　　　(92°,32°)

(a) Songpan-Ganzi

RMS misfit = 0.24

(b) Northern Lhasa

RMS misfit = 0.40
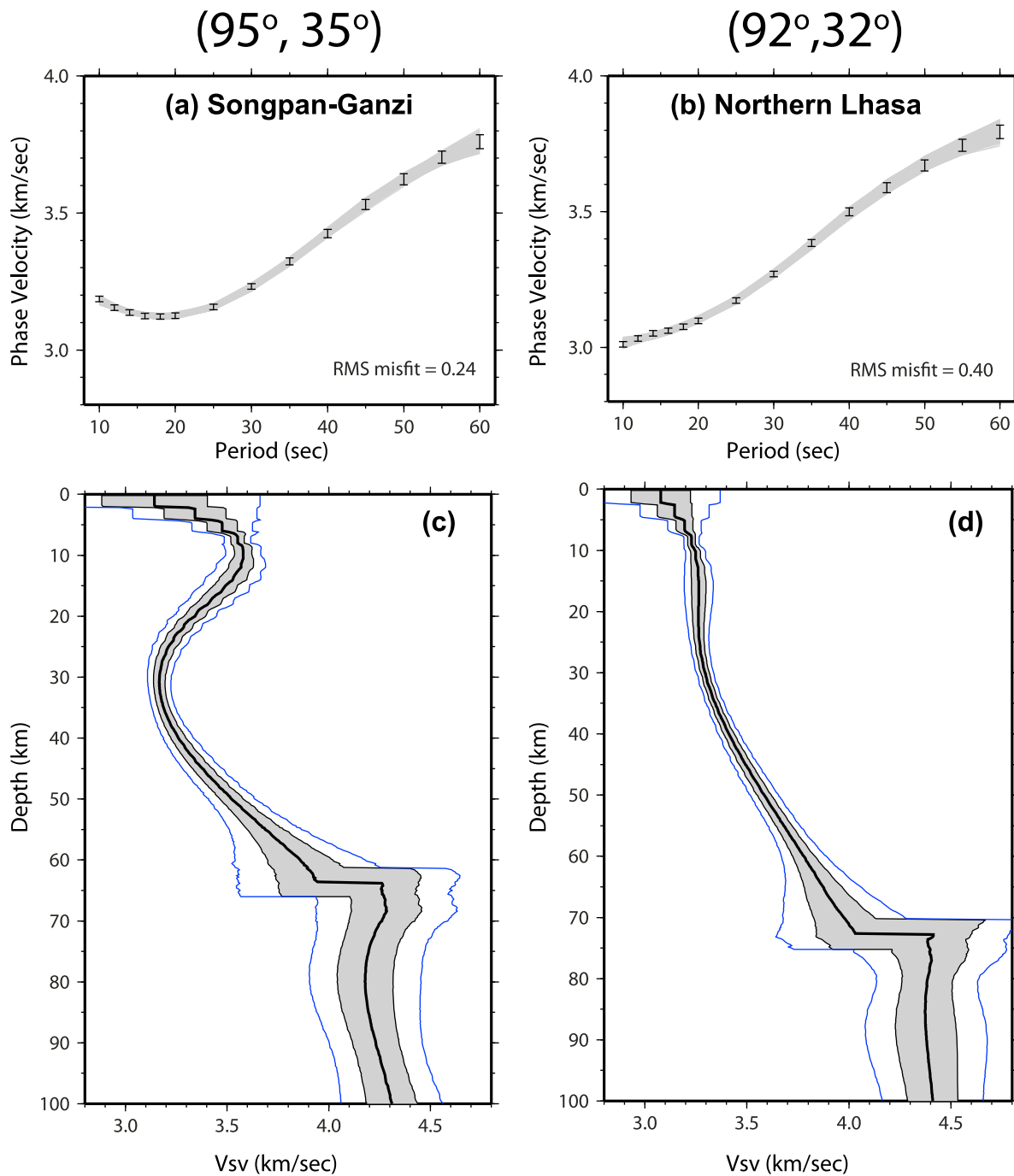
Figure 7. Examples of the Vsv inversion from phase velocity dispersion curves at locations a and b marked in Figure 1 as red and orange stars, respectively. (a) The observed Rayleigh wave phase velocity curve at location a presented with error bars. (b) Same as Figure 7a, but for position b. (c) The gray corridor identifies one standard deviation around the mean produced from the Monte-Carlo inversion. The blue lines mark two standard deviations around the mean. The black line is the average of the resulting ensemble of acceptable models from the Monte-Carlo inversion. (d) The same as Figure 7c, but for the dispersion curve presented in Figure 7b. The dispersion curves predicted from all of the models in the gray corridor are presented in Figures 7a and 7b as gray lines. The depths in Figures 7c and 7d are relative to the surface locally.

relative velocities to be computed, Figure 8 presents the regional average over the entire study area (blue line) as well as just across the Tibetan Plateau (red solid line). Shear wave speeds averaged across Tibet are lower than those averaged over the entire study region at all depths except in the top 10 km. The low velocities in the top 10 km averaged across the entire region result from the sedimentary basins surrounding Tibet. The mean shear velocity profile for Tibet
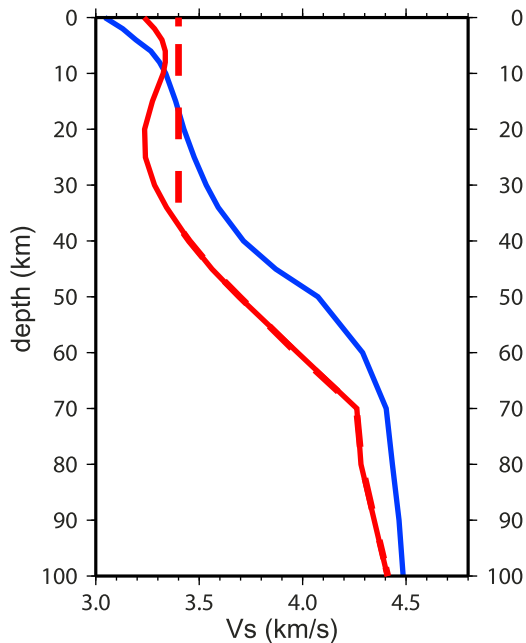
Figure 8. Several 1-D reference models: average model across the entire study region (solid blue line), average model across Tibet (solid red line), and average model across Tibet below 40 km depth but set equal to 3.4 km/s above 40 km (dashed red line). All depths are relative to sea level.

has a subtle low velocity zone in the middle crust from about 10 to 35 km depth with the minimum shear wave speed of ∼3.25 km/s appearing between depths of 20 and 25 km. The plots of relative shear velocities for the horizontal model slices shown in Figure 9 are taken relative to the regional average (blue line in Figure 8) with the uncertainties at corresponding depths plotted in Figure 10. Figure 11 presents absolute velocities in the vertical model profiles.

[29] The uncertainties of the 3-D Vs model are about 0.03–0.04 km/s (∼1%) in the upper and middle crust (Figures 10a–10c) except in sedimentary basins, such as the Tarim Basin, the Sichuan Basin, etc., where the uncertainties in the upper crust are larger due to the trade-off between sedimentary thickness and shear velocities in the upper crust. In the lower crust and uppermost mantle, the uncertainties increase significantly near the Moho discontinuity due to the trade-off between Moho depth and shear velocities in the neighboring depths, which is illustrated by the large uncertainties in the peripheries of northern and western Tibet at 55 km depth (Figure 10d) and almost in the whole of Tibet at 80 km depth (Figure 10e). In the upper mantle, more than 10 km deeper than the Moho, the uncertainties are ∼0.06–0.08 km/s, about twice as large as those in the upper/middle crust. The larger uncertainties in the upper mantle are due to the fact that the dispersion curves used to invert for the 3D model have periods shorter than 60 s, which have looser constraints on the upper mantle than on the crust.

[30] In the upper crust (5–15 km), the principal velocity features are the prominent low wave speeds of the sedimentary basins (Figure 9a), including the Tarim, Junggar, Qaidam and Sichuan Basins. Resolved sediments are seen clearly beneath the basins that appear as low elevation

features in Figure 11: A-A′, Tarim Basin; B-B′, Qaidam Basin; E-E′ and F-F′, Sichuan Basin. Low wave speeds are only present in the northern part of the Ordos block. The Qiangtang Terrane is slower than other parts of Tibet at 5 km depth. This is a region of Tibet with a relatively large number of irresolvable sedimentary basins that tend to be narrow in the north-south direction and elongated east-west (e.g., Fenghuo-Shan basins). Low wave speeds persist to 15 km depth beneath the Tarim, Junggar, and Qaidam basins (Figure 9b), whereas there are higher wave speeds in the Sichuan Basin, indicating that sediments in the Tarim, Junggar, and Qaidam basins are either thicker or considerably slower than those in the Sichuan Basin. The western Qiangtang Terrane has the slowest shear wave speeds across the entire region at 15 km depth. This is reflected in the westward shallowing of the crustal low velocity zone visible in profile D-D′ in Figure 11.

[31] Outside of Tibet at 30 km depth (Figure 9c), which is in the lower crust (Figure 9f), high velocities are imaged beneath all major basins including the Tarim, Qaidam, and Sichuan basins as well as the Ordos block. The lower crustal high velocities beneath the basins appear particularly clearly in the horizontal velocity profiles in Figure 11: A-A′, Tarim and Junggar basins; B-B′, Qaidam Basin; F-F′, Sichuan Basin. Such high velocity blocks are caused by cold and presumably strong lithosphere, not surprising for the Tarim and Sichuan basins that have impeded the outward growth and deformation of the Tibetan Plateau, which results in sharp topography along their boundaries. There are less pronounced high velocities beneath the Qaidam Basin, but this may result from the inability to resolve the anomaly fully in this smaller basin. At depths of 55 and 80 km, which are uppermost mantle depths outside of Tibet, the substructure of the basins remains fast and presumably strong, particularly for the Tarim Basin (Figure 11, A-A′) and the Sichuan Basin (Figure 11, E-E′, F-F′). This illustrates that the Tarim and Sichuan basins and the Ordos block are strong from the lower crust well into the mantle.

[32] Within Tibet at 30 km and 55 km depth (Figures 9c and 9d), which are in the middle and lower crust (Figure 9f), respectively, seismic wave speeds are generally slow compared to the surrounding regions (Figures 9c and 9d). At 30 km depth, this presumably reflects elevated temperatures and the state of deformation of the Tibet crust, but at 55 km depth the apparent low wave speeds within Tibet compared to the surrounding areas result mainly because this depth is a mantle depth for the areas outside of Tibet and, therefore, have upper mantle velocities. Wave speeds vary considerably across the plateau, however, as reflected by the somewhat patchy nature of the lowest wave speed anomalies observed in the central crust in Figure 11. The lowest wave speeds reside in northern Tibet mainly within the Qiangtang Terrane at 30 km depth but also extend into the Songpan-Ganzi Terrane. This low wave speed anomaly persists over the largest geographical area in Tibet, as seen in Figure 11, D-D′. The anomaly appears to be shifted slightly northward to span the Qiangtang and Songpan-Ganzi Terranes at 55 km. Because resolution degrades west of 95°E longitude (e.g., Figure 4), one must be cautious in interpreting the amplitude of anomalies in western Tibet. Beneath the low wave speed zone in the mid-crust beneath Tibet, seismic velocities increase quickly with depth from
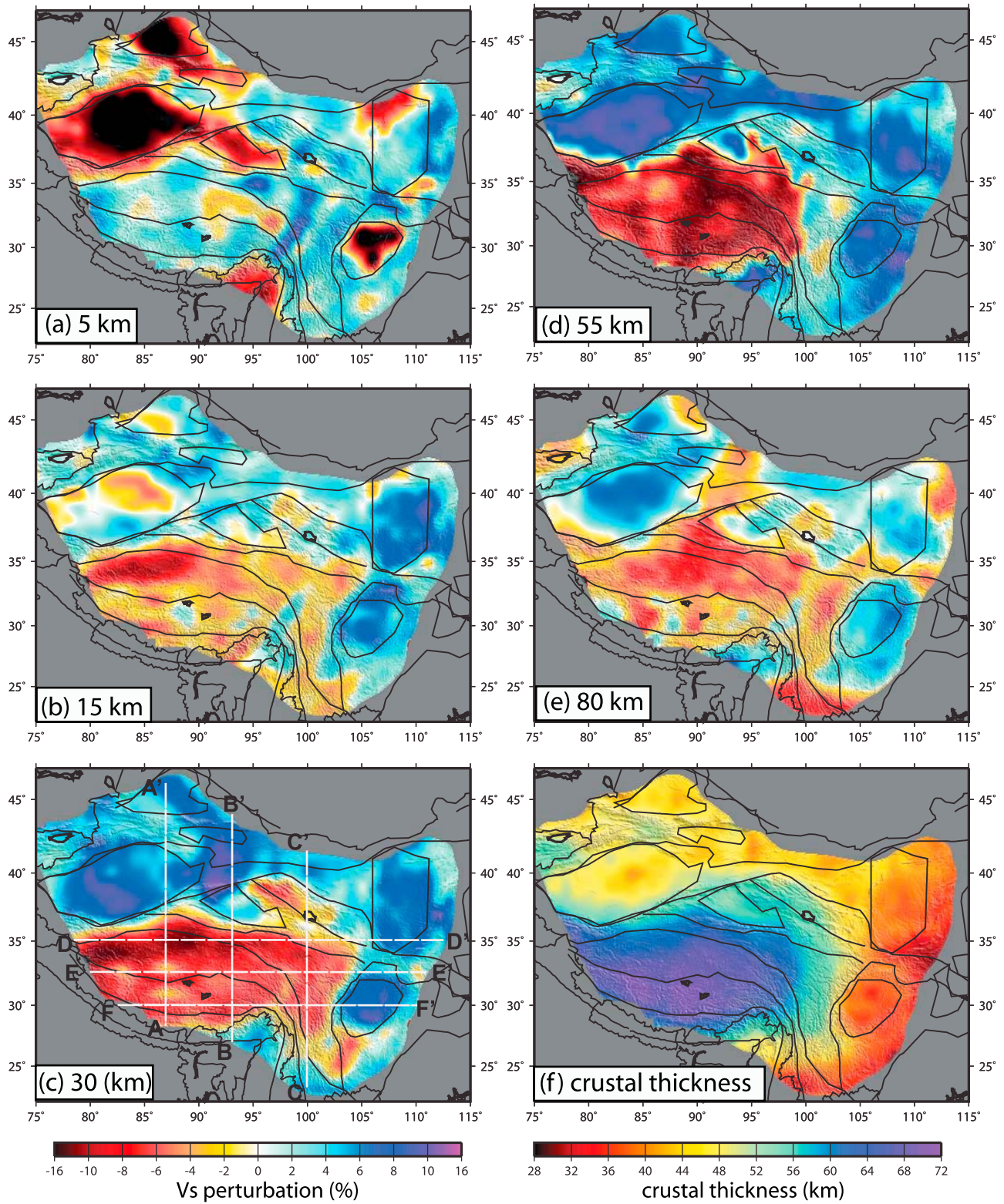
Figure 9. Vsv maps at depths of (a) 5, (b) 15, (c) 30, (d) 55 and (e) 80 km plotted as perturbations relative to the average across the entire region (blue line in Figure 8) at each depth. All depths are relative to sea level. Lines in Figure 9c delineate the locations of the vertical cross-sections shown in Figure 10. (f) Map of estimated crustal thickness.
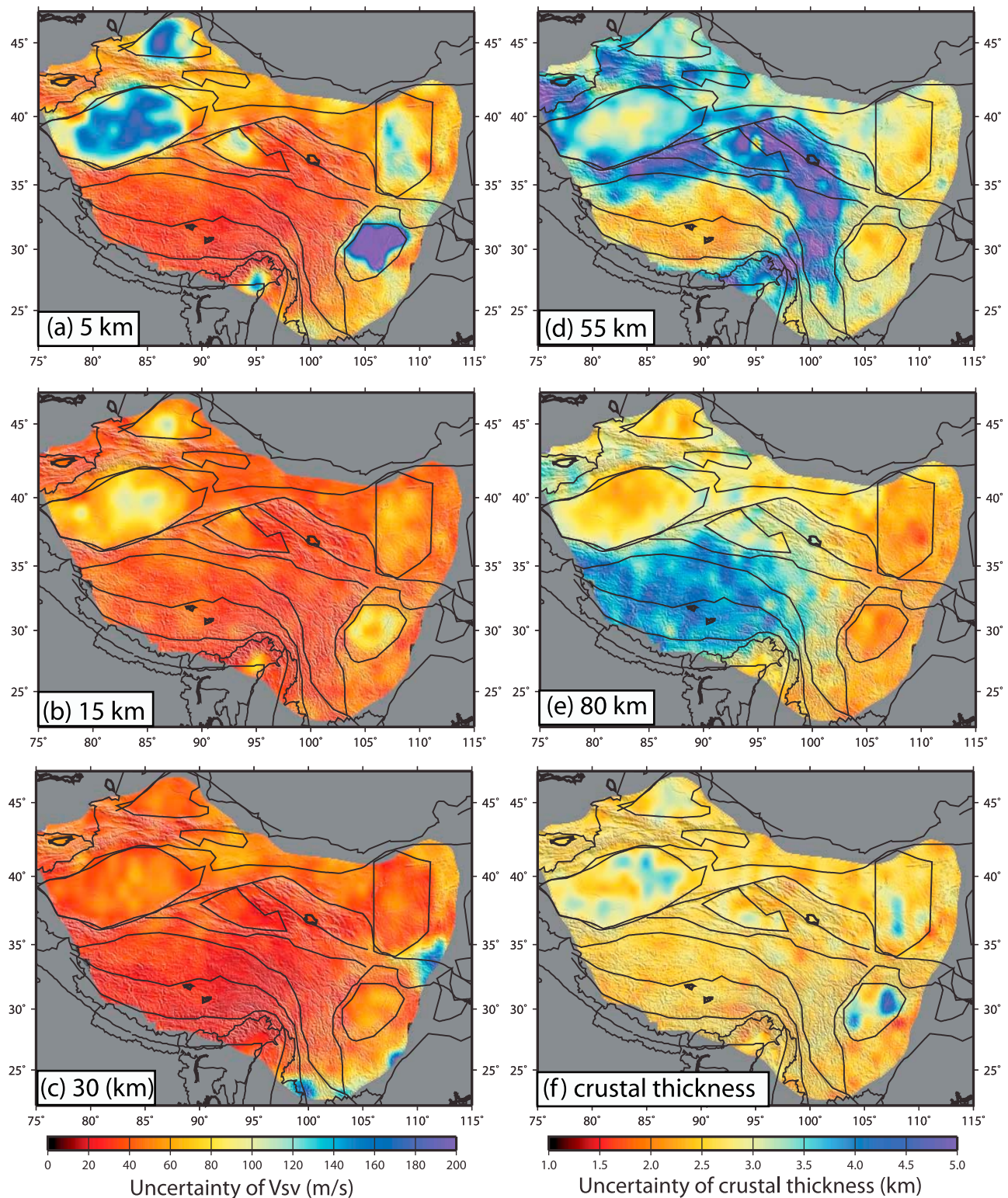
Figure 10. Maps of the uncertainties of the 3-D Vs model at depths of (a) 5, (b) 15, (c) 30, (d) 55 and (e) 80 km. (f) Uncertainties of crustal thickness.

about 3.5 km/s at 40 km depth to about 4.0 km/s at the Moho over a thickness of about 15–20 km.

[33] Estimated crustal thickness is presented in Figure 9f, but is not particularly well constrained with the data set used here and is largely reflective of the initial input model [*Shapiro and Ritzwoller*, 2002]. We note, however, that crustal thickness is greatest in southern Tibet and decreases in north Tibet consistent with the results of *Tseng et al.* [2009].
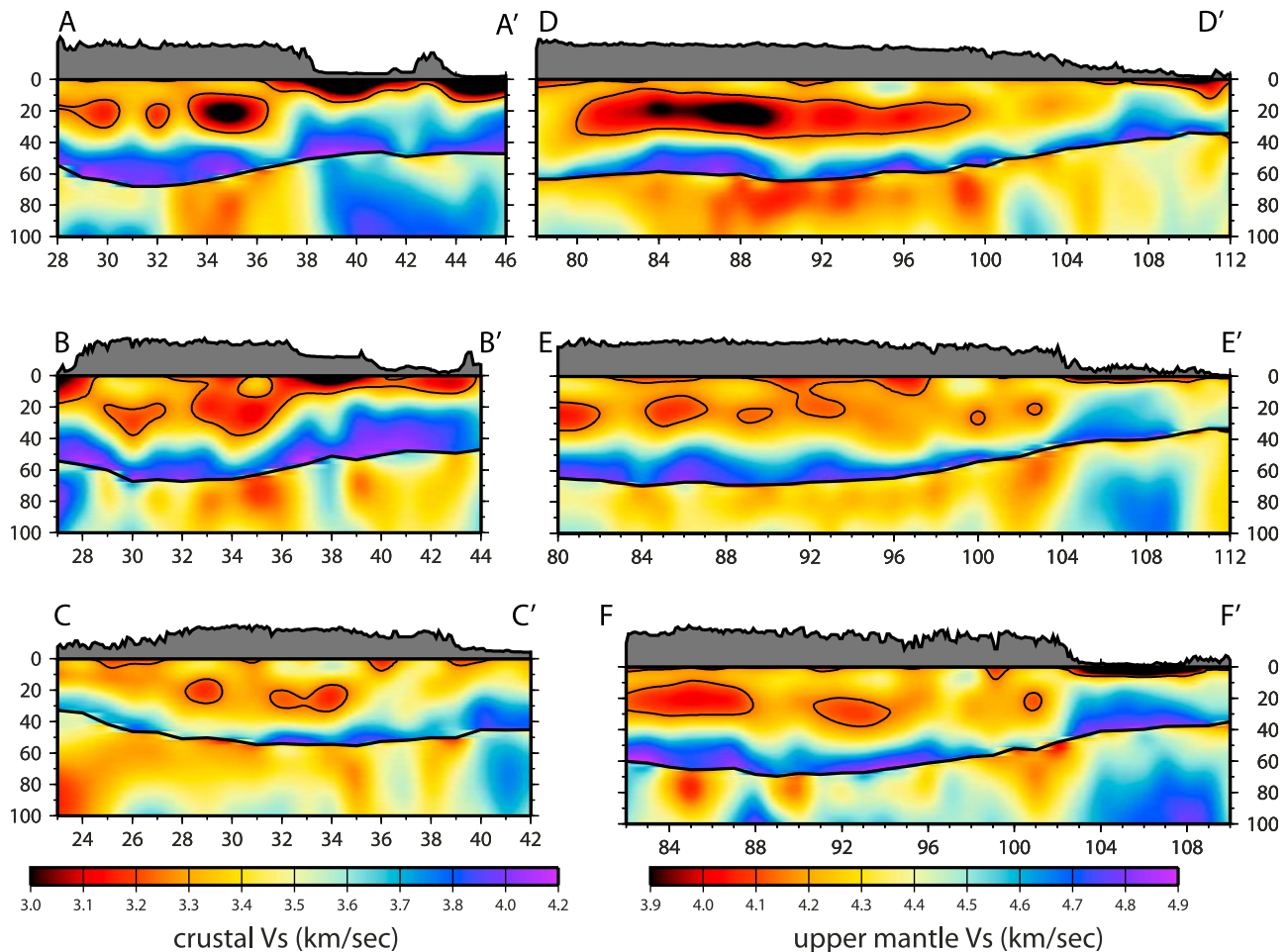
Figure 11. Vertical cross-sections of Vsv along the six profiles identified in Figure 9c. Surface topography is shown at the top of each panel. In contrast with Figure 9, shear wave speeds are presented in absolute units, but with different color scales in the crust and mantle. Very low shear wave speeds in the crust (<3.25 km/s) are encircled with black contours. All depths are relative to sea level.

[34] The uppermost mantle beneath Tibet (Figure 9e) is similarly slower than the surrounding regions and the lowest wave speed anomalies are also confined predominantly to the central Qiantang and Songpan-Ganzi Terranes. This is probably seen most clearly in Figure 11, profile A-A′. The mantle low velocity anomalies beneath Tibet, however, appear to be confined mostly to a relatively thin veneer of the uppermost mantle. Although evidence is not entirely clear from the model presented here, which extends only to 100 km depth, this observation is consistent with earlier studies that have observed low velocities in the shallow mantle underlain by higher velocities in the somewhat deeper uppermost mantle (e.g., *Villaseñor et al.* [2001], *Shapiro and Ritzwoller* [2002], *Acton et al.* [2010], and numerous others).

6. Discussion

6.1. Measuring the Amplitude of the Tibetan Crustal LVZ

[35] The 3-D Vs model discussed in the previous section exhibits prominent low shear wave speeds (Vsv) in the middle crust beneath much of Tibet between depths of 15 and 40 km with minimum speeds ranging between 2.9 and 3.3 km/s. To infer the existence of a crustal low velocity zone (LVZ) and measure its amplitude and distribution across the Tibetan crust, it is first necessary to define what is meant by a "low velocity zone."

[36] Many researchers would define a LVZ as a discrete depth range in which wave speeds are lower than at depths both above and below the range revealing a clear depth localized minimum in velocity. In this case, the existence of a LVZ would depend not just on the characteristics of the layer itself, but also on what lies above it. The profile in Figure 7c would satisfy this specification with the minimum of the LVZ at about 30 km depth, but the profile in Figure 7d would not. Yet, the shear wave speed at 30 km depth in Figure 7d is also quite low. Thus, if the interest is to identify depths where shear wave speeds are low enough possibly to reflect the presence of partial melt, then identifying the existence of low velocities is what is needed irrespective of the overlying layers. In this case, it would be appropriate to compare Vsv at 30 km depth with a single reference wave speed V_{ref}, perhaps representative of the speed at which partial melt is expected to appear at that depth. If, however, one wishes to identify regions in which channel flow may be most likely to occur, then it would be more appropriate to
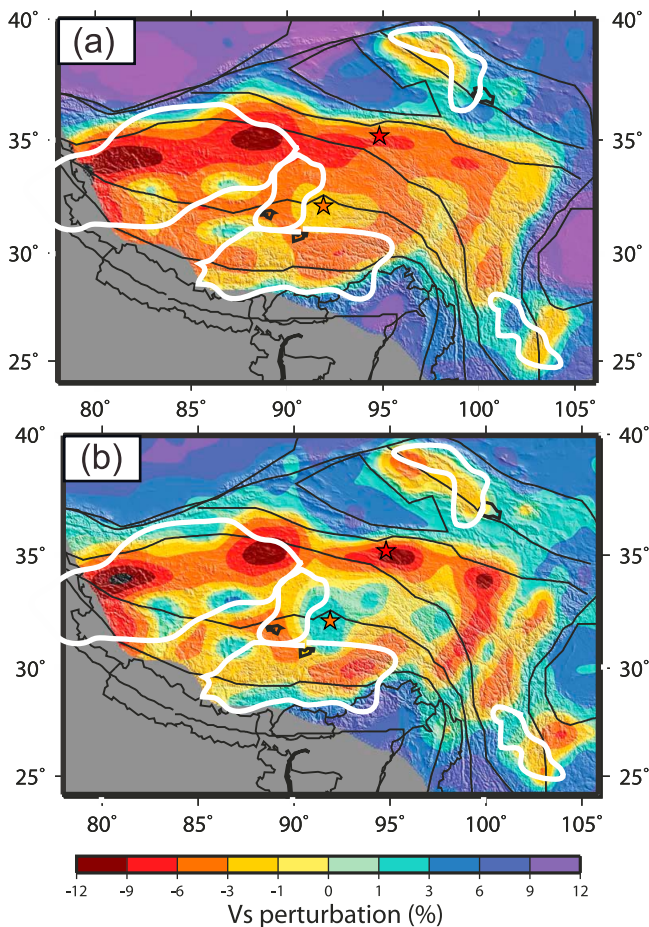
Figure 12. (a) Map of the amplitude of the crustal low velocity zone across the region based on the definition given by equation (1). Yellows, oranges, and reds denote velocities at 30 km depth (relative to sea level) less than 3.4 km/s (dashed red reference curve in Figure 8). (b) Same as Figure 12a, but with the definition of the amplitude of the crustal low velocity zone given by equation (2), which specifically measures a depth localized velocity minimum. White contours in Figures 12a and 12b identify strong radial anisotropy found in the study of *Shapiro et al.* [2004]. The colored stars denote the same locations as in Figure 1.

determine the minimum crustal velocity and compare it to the highest velocity in the layer that overlies it. The choice of definition depends on one's interest. Here, we will refer to both cases, however, as low velocity zones even though in the former case a vertically localized minimum of shear velocity may not exist in the middle crust.

[37] With this in mind, we present two different measurements of the amplitude of a LVZ. The first measurement is as follows:

$$LVZ_1 = \frac{V(30 \text{ km}) - V_{ref}}{V_{ref}} \quad (1)$$

With this definition, wave speeds below the threshold of V_{ref} would appear as negative. This definition will identify areas where shear wave speeds at 30 km depth are low and, hence, hold the potential for partial melt, assuming that partial melt

would set on at a wave speed of about V_{ref}. The second measurement of the amplitude of the LVZ is:

$$LVZ_2 = \frac{V(30 \text{ km}) - V_{max}(0–20 \text{ km})}{V_{ref}} \quad (2)$$

where $V_{max}(0–20 \text{ km})$ is the highest shear wave speed between the surface and 20 km depth. This definition specifically identifies regions with a vertically localized minimum shear wave speed which may reflect greater potential for channel flow.

[38] The reference wave speed, V_{ref}, appears in both definitions of the amplitude of a LVZ. The isotropic shear wave speed at which partial melt is expected to appear at 30 km depth beneath Tibet is difficult to determine with confidence because in situ temperature, composition, and water content are poorly known and probably variable across Tibet. *Christensen* [1996] presents shear wave velocities at 1000 MPa (~30 km depth) for a variety of solid, dry metamorphic rocks. Average values are about 3.65 km/s at room temperature. For a set of gneisses, *Kern et al.* [2001] find an average value of about −0.2 m/s/°C for the effect of temperature on the shear wave speed. *Litvinovsky et al.* [2000] argue that dry crustal rocks will not melt until about 900°C. Thus, dry crustal metamorphic rocks at 30 km depth would be expected to begin to melt at about 3.45 km/s. Wet rocks would begin to melt at lower temperatures (higher shear wave speeds), however. In this study, we set $V_{ref} = 3.40$ km/s. This is a reasonable but poorly constrained value below which the existence of partial melt would be plausible at 30 km depth. Figure 8 (red dashed line) also shows that it is the average value across Tibet at 40 km depth and in regions with a clear LVZ, like the Songpan-Ganzi Terrane location presented in Figure 7c, it is more or less the speed at the bottom of the LVZ (near 45 km depth).

[39] With the first definition of the amplitude of the LVZ presented in equation (1), which measures the shear wave speed at 30 km depth relative to the speed below which melt is reasonably expected to occur, the model profile from the Songpan-Ganzi Terrane (Figure 7c) has an amplitude of −6%, which is 6% below the speed at which melt may be expected to set on. The amplitude of the LVZ for the profile from the northern Lhasa Terrane in (Figure 7d) is about −2%. Both model profiles shown in Figure 7, therefore, have negative values with the first definition of the amplitude of the LVZ and are potentially consistent with the presence of partial melt in the middle crust. Partial melt at the Songpan-Ganzi location is more likely, however. Figure 12a uses this definition for the amplitude of the LVZ. Negative values are observed across most of Tibet, meaning that at 30 km depth most of Tibet has Vsv < 3.4 km/s. The largest negative values are found primarily in far northern Tibet.

[40] With the second definition of the amplitude of the LVZ given by equation (2), which accentuates regions with a mid-crustal shear velocity minimum, the amplitude at the Songpan-Ganzi Terrane location grows to about −10%. At the northern Lhasa Terrane location, however, the amplitude becomes positive, equal to about +3%. Thus, with this definition, a high amplitude LVZ is identified beneath the Songpan-Ganzi Terrane, but no LVZ exists beneath the northern Lhasa Terrane. Figure 12b uses this definition for

the amplitude of the LVZ and much of central Tibet does not have a LVZ. Rather, the LVZ is focused in a ring around the periphery of Tibet, with the largest amplitudes in northern Tibet.

6.2. The Distribution and Connectivity of LVZs in the Tibetan Middle Crust

[41] Although the two definitions of the amplitude of the LVZ beneath Tibet at 30 km depth provide somewhat different information about the details of the geometry of the LVZ, the general picture that emerges is coherent (Figures 12a and 12b) and has five principal characteristics. (1) Low velocities in the mid-crust exist across most of the high Tibetan Plateau. (2) The distribution of the amplitude of the LVZ is not uniform. In fact, the largest amplitudes (i.e., lowest mid-crustal shear wave speeds) are found predominantly around the periphery of Tibet. The largest amplitudes for the LVZ are in the western Qiangtang Terrane and the northern Songpan-Ganzi Terrane directly south of the Tarim and Qaidam basins. Large amplitudes are also observed in the southern Lhasa Terrane along the entire Himalayan front and in the eastern Songpan-Ganzi Terrane, where it turns the corner and is sandwiched between the Sichuan Basin and the Qiangtang Terrane. This region is sometimes further divided into the Bayan Har and Chuandian blocks, although these sub-regions are not specifically identified in Figure 1. (3) A LVZ characterized by a vertically localized minimum wave speed is found predominantly in the peripheral regions of Tibet. Strong anomalies (oranges and reds in Figure 12b) are coincident with locations where the Rayleigh wave dispersion curves have negative slopes below 15 s period as seen in Figure 6. Although low mid-crustal wave speeds can be found throughout much of Tibet, a low velocity minimum near 30 km depth is a feature found predominantly near the boundaries of Tibet. (4) Mid-crustal LVZs are large-scale features characterized by spatial continuity and connectivity, although there are variations in their amplitudes. (5) Mid-crustal LVZs cut across surface tectonic features within Tibet and, in particular, do not honor the surface expressions of faults at large scales. However, small-scale local features in faults or small-scale sharp velocity transitions across major faults could be smeared out or damped out in our tomography because our tomography has a resolution about 100–200 km.

6.3. Do LVZs in the Tibetan Middle Crust Imply the Presence of Partial Melt or Aqueous Fluids?

[42] A wide variety of geophysical evidence points to the existence of mechanically weak zones in the Tibetan crust. *Klemperer* [2006] presents an admirable review. *Caldwell et al.* [2009] argue compellingly that the low shear wave speeds (2.9–3.3 km/s) they observe beneath the northwest Himalaya at 30 km depth, which are similar to the speeds we observe across interconnected regions of Tibet on a much larger scale, are inconsistent with solid, dry crustal rocks of reasonable composition. Rather, they argue that dry rocks would not begin to melt until temperatures of greater than 900°C, which are unlikely at this depth across large regions of Tibet. Thus, they believe that such low shear velocities must result from partial melting that was enhanced or initiated by the existence of aqueous fluids. The existence of mid-crustal fluids has also been proposed to explain low-

resistivity magnetotelluric anomalies across southern and eastern Tibet [e.g., *Unsworth et al.*, 2005; *Bai et al.*, 2010], reflection bright spots [e.g., *Makovsky and Klemperer*, 1999], as well as other geological and geophysical data [e.g., *Kind et al.*, 1996; *Nelson et al.*, 1996; *Rapine et al.*, 2003]. Because rock strength depends on hydration state and the presence of partial melt [e.g., *Kirby*, 1984; *Rosenberg and Handy*, 2005], in addition to composition and temperature [e.g., *Afonso and Ranalli*, 2004], mid-crustal partial melt may reflect a strength minimum that would permit channel flow and the potential for partial or complete decoupling of flow from shallower to deeper levels [e.g., *Bird*, 1991; *Royden et al.*, 1997; *Beaumont et al.*, 2004]. It is, therefore, important to ask: Are the mid-crustal low velocity zones that we observe beneath Tibet caused by partial melt? If so, most researchers would probably agree that the observation would add substantial weight to the argument for channel flow across large regions of Tibet, even though a strength minimum would not necessitate vertical decoupling [e.g., *Klemperer*, 2006].

[43] In addressing this question, the effect of mineral alignment must be considered because it could significantly reduce the need for partial melt. Our study is based on Rayleigh waves, which are sensitive to vertically polarized shear wave speeds (Vsv) that may be slower than horizontally polarized shear speeds (Vsh). The velocity difference between Vsv and Vsh is referred to as radial anisotropy, which can be produced by horizontal shearing that preferentially aligns anisotropic minerals in the horizontal plane. Micas and amphibolites aligned through deformation are likely candidate anisotropic minerals in the middle crust beneath Tibet [e.g., *Mahan*, 2006; *Tatham et al.*, 2008]. In a large-scale tomographic study, *Shapiro et al.* [2004] mapped strong mid-crustal radial anisotropy in areas of Tibet where the moment tensors of earthquakes indicate active crustal thinning. They found that about 10% lower Vsv than Vsh is required beneath the high plateau to fit both Rayleigh and Love wave dispersion curves if the anisotropic layer is confined exclusively to the middle crust. *Duret et al.* [2010], through direct (non-tomographic) measurement of Rayleigh and Love wave group speed curves for wave paths that transit central Tibet from aftershocks of the 2008 Sichuan earthquake to western Tibet, measured radial anisotropy with 10–20% lower Vsv than Vsh in the middle crust. Their wave paths, however, did not pass through regions with the strongest LVZs in our study or strongest radial anisotropy in the study of *Shapiro et al.* [2004], implying that radial anisotropy estimated by *Shapiro et al.* [2004] may have been underestimated. A better estimate of the amplitude of radial anisotropy from *Shapiro et al.* [2004] may be between 10% and 20%.

[44] In order to compare the regions of strong radial anisotropy determined by *Shapiro et al.* [2004] with mid-crustal slow Vsv features, we outline the areas with strong radial anisotropy and superimpose them on the estimates of the amplitude of the LVZs using bold white contours in Figure 12. The distribution of strong radial anisotropy is largely coincident with strong LVZs in western and central Tibet. Agreement is weaker in eastern Tibet, but this is probably due to the reduction of resolution in this region in the study of *Shapiro et al.* [2004]. Radial anisotropy with 10–20% lower Vsv relative to Vsh implies 5–10% lower

Vsv relative to the effective isotropic shear velocity. A reduction in Vsv by about 5% at 30 km depth would absorb about half of the amplitude of the LVZs shown in Figure 12. A 10% reduction in Vsv would absorb most of the amplitude of the LVZs except in isolated patches. The potential for only isolated pockets of partial melt to exist has been considered by *Hetenyi et al.* [2011], who argue that crustal LVZs in southern Tibet are localized and discontinuous, being found predominantly beneath rifts and less commonly beneath grabens.

[45] We note that a recent model proposed by *Kawakatsu et al.* [2009] in which horizontal melt–rich layers are embedded in meltless mantle, can produce both a LVZ in Vsv and strong radial anisotropy in the oceanic asthenosphere. Thus, we ask: if there were similar horizontal melt–rich layers in the middle crust of Tibet, could they produce results consistent with our observations? Based exclusively on our Vsv model, we cannot rule out this possibility. But, if this horizontal melt–rich layer does exist, it will reduce both Vsv and Vsh, even though the reduction in Vsv will be stronger than Vsh. This would result in a LVZ comprising both Vsv and Vsh. Thus, an isotropic LVZ resulting from a horizontal melt-rich layers would be inconsistent with observations by *Duret et al.* [2010] who show monotonically increasing Vsh and isotropic shear velocity at least in the central Tibetan crust.

[46] However, the uncertainty of the amplitude of radial anisotropy makes a quantitative determination of the necessity for partial melt to explain the observed LVZs difficult. From the geographical coherence between the locations of the LVZs and strong radial anisotropy two conclusions are clear, however. The inferred horizontal alignment of anisotropic minerals in the middle crust (1) diminishes the need for partial melt and (2) makes any partial melt that does exist less inter-connected and distributed in more isolated patches – but still preferentially near the periphery of Tibet. To go beyond these qualitative conclusions, a study of Love wave dispersion like the present study is needed to deliver similar resolution about Vsh in the middle crust.

[47] Does this mean that no fluids exist now or in the past in the Tibetan middle crust? Radial anisotropy and mid-crustal fluids may, in fact, be intimately related as anisotropic minerals may require ambient aqueous fluids in order to form. Large bulk fractions of anisotropic minerals may form by retrograde metamorphism [e.g., *Mahan*, 2006] in which hydrous phases such as micas and amphiboles are formed when minerals in cooling rocks re-hydrate via interactions with external fluids. Thus, in a twist that further complicates interpretation, radial anisotropy actually may be a marker for the existence of current or past fluids in the middle crust.

6.4. Implications for Crustal Deformation and Crust-Mantle Coupling?

[48] A zone of partial melt restricted vertically to reside in the middle crust would have a significant impact on mid-crustal rheology. As discussed in the previous section, however, mineralogical alignment reflected in mid-crustal radial anisotropy would substantially (perhaps entirely) reduce the need for partial melt in the middle crust to explain the extensive, interconnected low velocity features that we observe here. As *Klemperer* [2006] notes, there are

significant differences in the information provided by observations of partial melt and mineralogical alignment. Whereas partial melt reflects current crustal weakness without demonstrating deformation, mineralogical alignment probably results from deformation but which may not be ongoing. *Shapiro et al.* [2004] argue that their observations of radial anisotropy reflect the integrated effects of past deformation of the middle crust beneath Tibet. We address two questions here qualitatively. (1) Are the higher resolution observations of mid-crustal Vsv low velocity zones that we present here and argue derive predominantly from mineralogical alignment reflective of deformation restricted to the middle crust? (2) Do the observations provide further evidence for the channel flow model of crustal deformation beneath Tibet and the de-coupling between the upper crustal and mantle deformation? We answer both questions in the negative.

[49] Strong crustal anisotropy requires two conditions to exist: the existence of anisotropic minerals and shear strains sufficient to align them. The observation of strong radial anisotropy beneath Tibet by *Shapiro et al.* [2004] and *Duret et al.* [2010] demonstrates that both conditions are met at least in parts of the Tibetan middle crust. The absence of radial anisotropy does not necessarily imply, however, that strains in the lower crust are different than those in the middle crust. Rather, anisotropic crustal minerals such as micas or amphiboles are notoriously sensitive to temperature, pressure, and fluid content. In particular, the thermodynamic stability of micas [*René et al.*, 2008] and amphibolites [e.g., *Spear*, 1981] suggests that these anisotropic crustal may be rare or absent in the Tibetan lower crust. Thus, the absence of lower-crustal radial anisotropy in the presence of mid-crustal anisotropy does not uniquely imply that strain or rheological conditions differ between the middle to lower crust. The inference of the vertical continuity or discontinuity of strain will depend (perhaps among other phenomena) on observations of azimuthal anisotropy in the crust and uppermost mantle at the resolutions presented here. These observations do not yet exist across all of Tibet. *Sol et al.* [2007] compare mantle azimuthal anisotropy with surface geological observations across southeastern Tibet from which they conclude the continuity of deformation between the crust and uppermost mantle. Ambient noise and earthquake tomography hold the promise to provide a unified model of azimuthal anisotropy in the crust and uppermost mantle that will solidify these inferences and extend them across all of Tibet.

[50] Finally, there is a robust observation presented here that motivates a question whose answer may yield significant information about the mode of deformation of the Tibetan crust. Why are the observed LVZs found predominantly near the periphery of Tibet? The answer to this question is beyond the scope of this paper, but it presents a geodynamical challenge that deserves further inquiry.

6.5. Evidence for an Eclogitic Layer in the Lower Crust?

[51] Based on the analysis of crustal xenoliths entrained in volcanic rocks from southern Tibet and the Qiangtang terrane [e.g., *Hacker et al.*, 2005; *Chan et al.*, 2009], *Searle et al.* [2011] proposed that the principal mineralogical composition of the Tibetan lower crust is granulite and

eclogite with some ultramafic restites. In addition, the P-T conditions of Miocene granulites from the xenoliths indicate a thick (60–80 km), hot (>900–1000°C) and dry lower crust. They also argue that the presence of eclogite-facies rocks and ultramafic restitic xenoliths supports an eclogitized lower crustal model. Based on laboratory measurements of monomineralic rocks, *Christensen* [1996] shows that the shear wave speed of eclogite at 1000 MPa (∼30 km depth) is ∼4.6 km/s at room temperature. *Jiménez-Munt et al.* [2008] estimate the temperature in the lower crust at depths greater than 40 km in Tibet typically ranges from 600 to 1000°C with the highest Moho temperature reaching up to ∼1150°C in the Qiangtang terrane according to thermodynamic modeling. If we assume the relationship of about −0.2 m/s/°C for the effect of temperature on the shear wave speed [*Kern et al.*, 2001] holds for eclogite, the shear wave speed of eclogite in the lower crust would be higher than ∼4.4 km/s, which is close to typical uppermost mantle shear wave speeds (Figures 7c and 7d).

[52] The observed shear wave speeds in the lowermost crust average about 4.00 km/s at 60 km depth beneath Tibet, with the highest average shear velocities reaching about 4.25 km/s directly above the Moho. Although these are fast shear wave speeds for the lower crust, they are still much lower than the shear wave speed expected for eclogite. This indicates that the lower crust may be only partially eclogitized if eclogitization does indeed occur. Similarly, *Schulte-Pelkum et al.* [2005] estimate ∼30% of the lower crust undergoes eclogitization in southern Tibet based on analyzing high P wave speeds in the lower crust of southern Tibet observed from studies of receiver functions. Their model shows that the high speed lower crust is principally limited to southern Tibet with the northern boundary around 31°N [*Nábelek et al.*, 2009], which has been interpreted as the partially eclogitized lower crust of India underthrusting southern Tibet. Our model presents consistently high lower crustal Vsv wave speeds beneath most of Tibet (e.g., Figures 7 and 11) that do not exhibit a notable difference between southern and northern Tibet. However, the shear wave speeds of the lower crust beneath western and central Tibet appear higher than those beneath eastern Tibet.

[53] As discussed earlier, our estimates of lower crustal wave speeds trade-off with uppermost mantle wave speeds, which is reflected in the increasing width of the corridor of accepted models near Moho in Figure 7. Moreover, the use of the B-spline parameterization in the crust imposes a strict vertical smoothness constraint that militates against large lower crustal velocities. Thus, we are not able to constrain the fraction of eclogitization in the lower crust precisely. Nevertheless, our model reveals a strong vertical gradient in shear wave speeds at depths greater than 40 km, which probably reflects a vertical compositional gradient in the lower Tibetan crust, consistent with a partially eclogitized lower crustal model. The introduction of receiver functions in the inversion with surface wave dispersion will help to improve the reliability of the model in the lowermost crust, which will be undertaken in a future study.

7. Conclusions

[54] Based on 1–2 years of continuous observations of seismic ambient noise at more than 600 stations in and around Tibet, we present Rayleigh wave phase velocity maps from 10 s to 60 s period and a 3-D Vsv model of the crust and uppermost mantle derived from these maps. The 3-D model exhibits significant apparently interconnected low shear velocity features across most of the Tibetan middle crust at depths between 20 and 40 km. These low velocity zones (LVZs) do not conform to surface faults and are most prominent near the periphery of Tibet.

[55] It is tempting to attribute the LVZs to the existence of mid-crustal partial melting perhaps initiated by the presence of aqueous fluids [e.g., *Caldwell et al.*, 2009]. However, previous estimates by *Shapiro et al.* [2004] of the location of strong radial anisotropy in the Tibetan middle crust caused by anisotropic minerals aligned by deformation are nearly coincident with the LVZs in central and western Tibet. (Agreement is weaker in eastern Tibet where resolution degrades in the study of Shapiro et al.) As *Duret et al.* [2010] discuss, the amplitude of radial anisotropy is not well determined in the global-scale tomographic study of *Shapiro et al.* [2004]. Thus, it is difficult to determine if the Vsv low velocity features that we observe are entirely or only partially the consequence of anisotropic mineral alignment in the middle crust. Whether the observed LVZs are caused by partial melt, the alignment of anisotropic minerals, or a combination of the two, they almost certainly identify areas of substantial past deformation that may still be ongoing. Therefore, a significant question arises from these observations: Why are the LVZs strongest near the periphery of Tibet? We do not propose to answer this question here but believe that its answer may provide information about the mode of deformation of the Tibetan crust.

[56] The fact that the LVZs do not honor surface faults is at variance with the "rigid block" model of deformation and provides direct support for the "internal deformation" model. Observations of LVZs confined to the middle crust may appear to support internal deformation via ductile "channel flow." However, if the LVZs are caused primarily by mineral alignment, then the lack of radial anisotropy in the lower crust may simply reflect the paucity of lower crustal anisotropic minerals. Until other specific seismic observations are made, LVZs observed in the middle crust based solely on Rayleigh waves cannot be used as an argument for the "channel flow" model. There are two specific seismic observations that are needed to extend and clarify inferences from the results presented here. First, higher resolution Love wave phase velocity measurements obtained from ambient noise across all of Tibet are needed to infer Vsh in the middle crust. These observations will help to determine whether the observed LVZs result entirely or only partially from mineral alignment. Second, azimuthal anisotropy observed both for the crust from ambient noise and uppermost mantle from earthquake records will constrain the vertical continuity of strain that will help to adjudicate between channel flow and vertically coherent deformation lacking in present observations.

References

Acton, C. E., K. Priestley, V. K. Gaur, and S. S. Rai (2010), Group velocity tomography of the Indo-Eurasian collision zone, *J. Geophys. Res.*, 115, B12335, doi:10.1029/2009JB007021.

Afonso, J. C., and G. Ranalli (2004), Crustal and mantle strengths in continental lithosphere: Is the jelly sandwich model obsolete?, *Tectonophysics*, 394, 221–232, doi:10.1016/j.tecto.2004.08.006.

Alsdorf, D., and D. Nelson (1999), Tibetan satellite magnetic low: Evidence for widespread melt in the Tibetan crust?, *Geology*, 27(10), 943–946, doi:10.1130/0091-7613(1999)027<0943:TSMLEF>2.3.CO;2.

Avouac, J.-P., and P. Tapponnier (1993), Kinematic model of active deformation in central Asia, *Geophys. Res. Lett.*, 20, 895–898, doi:10.1029/93GL00128.

Bai, D., et al. (2010), Crustal deformation of the eastern Tibetan plateau revealed by magnetotelluric imaging, *Nat. Geosci.*, 3, 358–362, doi:10.1038/ngeo830.

Barmin, M. P., M. H. Ritzwoller, and A. L. Levshin (2001), A fast and reliable method for surface wave tomography, *Pure Appl. Geophys.*, 158(8), 1351–1375, doi:10.1007/PL00001225.

Beaumont, C., R. A. Jamieson, M. H. Nguyen, and S. Medvedev (2004), Crustal channel flows: 1. Numerical models with applications to the tectonics of the Himalayan–Tibetan orogen, *J. Geophys. Res.*, 109, B06406, doi:10.1029/2003JB002809.

Bensen, G. D., M. H. Ritzwoller, M. P. Barmin, A. L. Levshin, F. Lin, M. P. Moschetti, N. M. Shapiro, and Y. Yang (2007), Processing seismic ambient noise data to obtain reliable broad-band surface wave dispersion measurements, *Geophys. J. Int.*, 169, 1239–1260, doi:10.1111/j.1365-246X.2007.03374.x.

Bird, P. (1991), Lateral extrusion of lower crust from under high topography, in the isostatic limit, *J. Geophys. Res.*, 96, 10,275–10,286, doi:10.1029/91JB00370.

Caldwell, W. B., S. L. Klemperer, S. S. Rai, and J. F. Lawrence (2009), Partial melt in the upper-mantle crust of the northwest Himalaya revealed by Rayleigh wave dispersion, *Tectonophysics*, 477, 58–65, doi:10.1016/j.tecto.2009.01.013.

Chan, G. H.-N., et al. (2009), Probing the basement of southern Tibet: Evidence from crustal xenoliths entrained in a Miocene ultrapotassic dyke, *J. Geol. Soc.*, 166, 45–52, doi:10.1144/0016-76492007-145.

Christensen, N. I. (1996), Poisson's ratio and crustal seismology, *J. Geophys. Res.*, 101(B2), 3139–3156, doi:10.1029/95JB03446.

Christensen, N. I., and W. D. Mooney (1995), Seismic velocity structure and composition of the continental crust: A global view, *J. Geophys. Res.*, 100(B6), 9761–9788, doi:10.1029/95JB00259.

Chu, R., L. Zhu, and D. V. Helmberger (2009), Determination of earthquake focal depths and source time functions in central Asia using teleseismic *P* waveforms, *Geophys. Res. Lett.*, 36, L17317, doi:10.1029/2009GL039494.

Chung, S.-L., et al. (2005), Tibetan tectonic evolution inferred from spatial and temporal variations in post-collisional magmatism, *Earth Sci. Rev.*, 68, 173–196, doi:10.1016/j.earscirev.2004.05.001.

Clark, M. K., and L. H. Royden (2000), Topographic ooze: Building the eastern margin of Tibet by lower crustal flow, *Geology*, 28, 703–706, doi:10.1130/0091-7613(2000)28<703:TOBTEM>2.0.CO;2.

Cotte, N., H. Pederson, M. Campillo, J. Mars, J. F. Ni, R. Kind, E. Sondvol, and W. Zhao (1999), Determination of the crustal structure in southern Tibet by dispersion and amplitude analysis of Rayleigh waves, *Geophys. J. Int.*, 138, 809–819, doi:10.1046/j.1365-246x.1999.00927.x.

Duret, F., N. M. Shapiro, Z. Cao, V. Leshin, P. Molnar, and S. Roecker (2010), Surface wave dispersion across Tibet: Direct evidence for radial anisotropy in the crust, *Geophys. Res. Lett.*, 37, L16306, doi:10.1029/2010GL043811.

Dziewonski, A. M., and D. L. Anderson (1981), Preliminary reference Earth model, *Phys. Earth Planet. Inter.*, 25(4), 297–356.

England, P., and G. Houseman (1986), Finite strain calculations of continental deformation: Comparison with the India-Asia collision zone, *J. Geophys. Res.*, 91, 3664–3676, doi:10.1029/JB091iB03p03664.

England, P., and P. Molnar (1997), Active deformation of Asia: From kinematics to dynamics, *Science*, 278, 647–650, doi:10.1126/science.278.5338.647.

Flesch, L. M., W. E. Holt, P. G. Silver, M. Stephenson, C.-Y. Wang, and W. W. Chan (2005), Constraining the extent of crust-mantle coupling in central Asia using GPS, geologic, and shear-wave splitting data, *Earth Planet. Sci. Lett.*, 238, 248–268, doi:10.1016/j.epsl.2005.06.023.

Guo, Z., X. Gao, H. Yao, J. Li, and W. Want (2009), Midcrustal low-velocity layer beneath the central Himalaya and southern Tibet revealed by ambient noise array tomography, *Geochem. Geophys. Geosyst.*, 10, Q05007, doi:10.1029/2009GC002458.

Hacker, B., et al. (2005), Near ultrahigh pressure processing of continental crust: Miocene crustal xenoliths from the Pamir, *J. Petrol.*, 46, 1661–1687, doi:10.1093/petrology/egi030.

Hetenyi, G., J. Vergne, L. Bollinger, and R. Cattin (2011), Discontinuous low velocity zones in southern Tibet question the viability of the channel flow model, in *Growth and Collapse of the Tibetan Plateau*, edited by R. Gloaguen and L. Ratschbacher, *Geol. Soc. Spec. Publ.*, 353, 99–108.

Huang, H., H. Yao, and R. D. van der Hilst (2010), Radial anisotropy in the crust in SE Tibet and SW China from ambient noise interferometry, *Geophys. Res. Lett.*, 37, L21310, doi:10.1029/2010GL044981.

Jiang, M., S. Zhou, E. Sandvol, X. Chen, X. Liang, Y. J. Chen, and W. Fan (2011), 3-D lithospheric structure beneath southern Tibet from Rayleigh-wave tomography with a 2-D seismic array, *Geophys. J. Int.*, 185, 593–608, doi:10.1111/j.1365-246X.2011.04979.x.

Jiménez-Munt, I., M. Fernàndez, J. Vergés, and J. P. Platt (2008), Lithosphere structure underneath the Tibetan plateau inferred from elevation, gravity and geoid anomalies, *Earth Planet. Sci. Lett.*, 267, 276–289, doi:10.1016/j.epsl.20078.11.045.

Kanamori, H. and D. Anderson (1977), Importance of physical dispersion in surface wave and free oscillation problems: Review, *Rev. Geophys.*, 15(1), 105–112, doi:10.1029/RG015i001p00105.

Kawakatsu, H., P. Kumar, Y. Takei, M. Shinohara, T. Kanazawa, E. Araki, and K. Suyehiro (2009), Seismic evidence for sharp lithosphere-asthenosphere boundaries of oceanic plates, *Science*, 324, 499–502.

Kern, H., T. Popp, F. Gorbatsevich, A. Zharikov, K. V. Lobanov, and Y. P. Smirnov (2001), Pressure and temperature dependence of VP and VS in rocks from the superdeep well and from surface analogues at Kola and the nature of velocity anisotropy, *Tectonophysics*, 338(2), 113–134, doi:10.1016/S0040-1951(01)00128-7.

Kind, R., et al. (1996), Evidence from earthquake data for a partially molten crustal layer in southern Tibet, *Science*, 274, 1692–1694, doi:10.1126/science.274.5293.1692.

Kirby, S. (1984), Introduction and digest to the special issue on chemical effects of water on the deformation and strengths of rocks, *J. Geophys. Res.*, 89, 3991–3995, doi:10.1029/JB089iB06p03991.

Klemperer, S. L. (2006), Crustal flow in Tibet: Geophysical evidence for the physical state of Tibetan lithosphere, and inferred patterns of active flow, in *Channel Flow, Ductile Extrusion and Exhumation in Continental Collision Zones*, edited by R. D. Law, M. P. Searle, and L. Godin, *Geol. Soc. Spec. Publ.*, 268, 39–70.

Levshin, A. L., X. Yang, M. P. Barmin, and M. H. Ritzwoller (2010), Mid-period Rayleigh wave attenuation model for Asia, *Geochem. Geophys. Geosyst.*, 11, Q08017, doi:10.1029/2010GC003164.

Li, H., W. Su, C.-Y. Wang, and Z. Huang (2009), Ambient noise Rayleigh wave tomography in western Sichuan and eastern Tibet, *Earth Planet. Sci. Lett.*, 282, 201–211, doi:10.1016/j.epsl.2009.03.021.

Lin, F., M. P. Moschetti, and M. H. Ritzwoller (2008), Surface wave tomography of the western United States from ambient seismic noise: Rayleigh and Love wave phase velocity maps, *Geophys. J. Int.*, 173, 281–298, doi:10.1111/j.1365-246X.2008.03720.x.

Lin, F.-C., M. H. Ritzwoller, and R. Snieder (2009), Eikonal tomography: Surface wave tomography by phase-front tracking across a regional broad-band seismic array, *Geophys. J. Int.*, 177(3), 1091–1110, doi:10.1111/j.1365-246X.2009.04105.x.

Litvinovsky, B. A., I. M. Steele, and S. M. Wickham (2000), Silicic magma formation in overthickened crust: Melting of charnockite and leucogranite at 15, 20 and 25 kbar, *J. Petrol.*, 41(5), 717–737, doi:10.1093/petrology/41.5.717.

Mahan, K. H. (2006), Retrograde mica in deep crustal granulites: Implications for crustal seismic anisotropy, *Geophys. Res. Lett.*, 33, L24301, doi:10.1029/2006GL028130.

Makovsky, Y., and S. L. Klemperer (1999), Measuring the seismic properties of Tibetan bright spots: Free aqueous fluids in the Tibetan middle crust, *J. Geophys. Res.*, 104, 10,795–10,825, doi:10.1029/1998JB900074.

Makovsky, Y., S. L. Klemperer, and L. Ratschbacher (1999), Midcrustal reflector on INDEPTH wide-angle profiles: An ophiolitic slab beneath the India–Asia suture in southern Tibet?, *Tectonics*, 18, 793–808, doi:10.1029/1999TC900022.

Molnar, P. (1988), A review of geophysical constraints on the deep structure of the Tibetan Plateau, the Himalaya, and the Karakorum and their tectonic implications, *Philos. Trans. R. Soc. London, Ser. A*, *326*, 33–88, doi:10.1098/rsta.1988.0080.

Moschetti, M. P., M. H. Ritzwoller, and N. M. Shapiro (2007), Surface wave tomography of the western United States from ambient seismic noise: Rayleigh wave group velocity maps, *Geochem. Geophys. Geosyst.*, *8*, Q08010, doi:10.1029/2007GC001655.

Mosegaard, K., and A. Tarantola (1995), Monte Carlo sampling of solutions to inverse problems, *J. Geophys. Res.*, *100*(B7), 12,431–12,447, doi:10.1029/94JB03097.

Nábelek, J., G. Hetényi, J. Vergne, S. Sapkota, B. Kafle, M. Jiang, H. Su, J. Chen, B.-S. Huang, and the Hi-CLIMB Team (2009), Underplating in the Himalaya-Tibet collision zone revealed by the Hi-CLIMB experiment, *Science*, *325*(5946), 1371–1374, doi:10.1126/science.1167719.

Nelson, K. D., et al. (1996), Partially molten middle crust beneath southern Tibet: Synthesis of Project INDEPTH results, *Science*, *274*, 1684–1688, doi:10.1126/science.274.5293.1684.

Rai, S. S., A. Ashish, A. Padhi, and P. R. Sarma (2009), High crustal seismic attenuation in Ladakh-Karakoram, *Bull. Seismol. Soc. Am.*, *99*(1), 407–415, doi:10.1785/0120070261.

Rapine, R., F. Tilmann, M. West, J. Ni, and A. Rodgers (2003), Crustal structure of northern and southern Tibet from surface wave dispersion analysis, *J. Geophys. Res.*, *108*(B2), 2120, doi:10.1029/2001JB000445.

René, M., F. Holz, C. Luo, O. Beermann, and J. Stelling (2008), Biotite stability in peraluminous granitic melts: Compositional dependence and application to the generation of two-mica granites in the South Bohemian batholith (Bohemian Massif, Czech Republic), *Lithos*, *102*(3–4), 538–553, doi:10.1016/j.lithos.2007.07.022.

Ritzwoller, M. H., and A. L. Levshin (1998), Eurasian surface wave tomography: Group velocities, *J. Geophys. Res.*, *103*, 4839–4878, doi:10.1029/97JB02622.

Ritzwoller, M. H., A. L. Levshin, L. I. Ratnikova, and A. A. Egorkin (1998), Intermediate period group velocity maps across central Asia, western China, and parts of the Middle East, *Geophys. J. Int.*, *134*, 315–328.

Ritzwoller, M. H., F. C. Lin, and W. Shen (2011), Ambient noise tomography with a large seismic array, *C. R. Geosci.*, *343*(8), 558–570.

Rosenberg, C. L., and M. R. Handy (2005), Experimental deformation of partially melted granite revisited: Implications for the continental crust, *J. Metamorph. Geol.*, *23*, 19–28, doi:10.1111/j.1525-1314.2005.00555.x.

Royden, L. H., B. C. Burchfiel, R. W. King, E. Wang, Z. Chen, F. Shen, and Y. Liu (1997), Surface deformation and lower crustal flow in eastern Tibet, *Science*, *276*, 788–790, doi:10.1126/science.276.5313.788.

Saito, M. (1988), DISPER80: A subroutine package for the calculation of seismic normal-mode solutions, in *Seismological Algorithms: Computational Methods and Computer Programs*, edited by D. Doornbos, pp. 293–319, Academic, San Diego, Calif.

Schulte-Pelkum, V., G. Monsalve, A. F. Sheehan, M. Pandey, S. Sapkota, R. Bilham, and F. Wu (2005), Imaging the Indian subcontinent beneath the Himalaya, *Nature*, *435*, 1222–1225, doi:10.1038/nature03678.

Searle, M. P., J. R. Elliott, R. J. Phillips, and S.-L. Chung (2011), Crustal-lithosphere structure and continental extrusion of Tibet, *J. Geol. Soc.*, *168*, 633–672, doi:10.1144/0016-76492010-139.

Shapiro, N. M., and M. H. Ritzwoller (2002), Monte-Carlo inversion for a global shear velocity model of the crust and upper mantle, *Geophys. J. Int.*, *151*, 88–105, doi:10.1046/j.1365-246X.2002.01742.x.

Shapiro, N. M., M. H. Ritzwoller, P. Molnar, and V. Levin (2004), Thinning and flow of Tibetan crust constrained by seismic anisotropy, *Science*, *305*, 233–236, doi:10.1126/science.1098276.

Sloan, R. A., J. A. Jackson, D. McKenzie, and K. Priestley (2011), Earthquake depth distributions in central Asia, and their relations with lithospheric thickness, shortening and extension, *Geophys. J. Int.*, *185*, 1–29, doi:10.1111/j.1365-246X.2010.04882.x.

Sol, S., et al. (2007), Geodynamics of the southeastern Tibetan Plateau from seismic anisotropy and geodesy, *Geology*, *35*, 563–566, doi:10.1130/G23408A.1.

Spear, F. (1981), An experimental study of hornblende stability and compositional instability of amphibolite, *J. Sci.*, *281*, 697–734.

Tatham, D. J., G. E. Lloyd, R. W. H. Butler, and M. Casey (2008), Amphibole and lower crustal seismic properties, *Earth Planet. Sci. Lett.*, *267*(1–2), 118–128, doi:10.1016/j.epsl.2007.11.042.

Tseng, T.-L., W.-P. Chen, and R. L. Nowack (2009), Northward thinning of Tibetan crust revealed by virtual seismic profiles, *Geophys. Res. Lett.*, *36*, L24304, doi:10.1029/2009GL040457.

Unsworth, M. J., A. G. Jones, W. Wei, G. Marquis, S. G. Gokarn, J. E. Spratt, and the INDEPTH-MT Team (2005), Crustal rheology of the Himalaya and Southern Tibet inferred from magnetotelluric data, *Nature*, *438*, 78–81, doi:10.1038/nature04154.

Villaseñor, A., M. H. Ritzwoller, A. L. Levshin, M. P. Barmin, E. R. Engdahl, W. Spakman, and J. Trampert (2001), Shear velocity structure of central Eurasia from inversion of surface wave velocities, *Phys. Earth Planet. Inter.*, *123*(2–4), 169–184, doi:10.1016/S0031-9201(00)00208-9.

Xie, J. (2004), Lateral variations of crustal seismic attenuation along the INDEPTH profiles in Tibet from *Lg Q* inversion, *J. Geophys. Res.*, *109*, B10308, doi:10.1029/2004JB002988.

Xu, L., S. Rondenay, and R. D. van der Hilst (2007), Structure of the crust beneath the southeastern Tibetan Plateau from teleseismic receiver functions, *Phys. Earth Planet. Inter.*, *165*, 176–193, doi:10.1016/j.pepi.2007.09.002.

Yang, Y., and D. W. Forsyth (2006), Rayleigh wave phase velocities, small-scale convection and azimuthal anisotropy beneath southern California, *J. Geophys. Res.*, *111*, B07306, doi:10.1029/2005JB004180.

Yang, Y., M. H. Ritzwoller, A. L. Levshin, and N. M. Shapiro (2007), Ambient noise Rayleigh wave tomography across Europe, *Geophys. J. Int.*, *168*(1), 259–274, doi:10.1111/j.1365-246X.2006.03203.x.

Yang, Y., A. Li, and M. H. Ritzwoller (2008a), Crustal and uppermost mantle structure in southern Africa revealed from ambient noise and teleseismic tomography, *Geophys. J. Int.*, *174*, 235–248, doi:10.1111/j.1365-246X.2008.03779.x.

Yang, Y., M. H. Ritzwoller, F.-C. Lin, M. P. Moschetti, and N. M. Shapiro (2008b), The structure of the crust and uppermost mantle beneath the western United States revealed by ambient noise and earthquake tomography, *J. Geophys. Res.*, *113*, B12310, doi:10.1029/2008JB005833.

Yang, Y., et al. (2010), Rayleigh wave phase velocity maps of Tibet and the surrounding regions from ambient seismic noise tomography, *Geochem. Geophys. Geosyst.*, *11*, Q08010, doi:10.1029/2010GC003119.

Yao, H., C. Beghein, and R. D. van der Hist (2008), Surface wave array tomography in SE Tibet from ambient seismic noise and two-station analysis: II. Crustal and upper-mantle structure, *Geophys. J. Int.*, *173*, 205–219, doi:10.1111/j.1365-246X.2007.03696.x.

Yao, H., R. D. van der Hilst, and J.-P. Montagner (2010), Heterogeneity and anisotropy of the lithosphere of SE Tibet from surface wave array tomography, *J. Geophys. Res.*, *115*, B12307, doi:10.1029/2009JB007142.

Zheng, S., X. Sun, X. Song, Y. Yang, and M. H. Ritzwoller (2008), Surface wave tomography of China from ambient seismic noise correlation, *Geochem. Geophys. Geosyst.*, *9*, Q05020, doi:10.1029/2008GC001981.

Zheng, X. F., B. Ouyang, D. N. Zhang, Z. X. Yao, J. H. Liang, and J. Zheng (2009), Technical system construction of Data Backup Centre for China Seismograph Network and the data support to researches on the Wenchuan earthquake [in Chinese with English abstract], *Chin. J. Geophys.*, *52*(5), 1412–1417, doi:10.3969/j.issn.0001-5733.2009.05.031.

Zheng, X. F., Z. X. Yao, J. H. Liang, and J. Zheng (2010), The role played and opportunities provided by IGP DMC of China National Seismic Network in Wenchuan earthquake disaster relief and research, *Bull. Seismol. Soc. Am.*, *100*(5B), 2866–2872, doi:10.1785/0120090257.

Zheng, Y., W. Shen, L. Zhou, Y. Yang, Z. Xie, and M. H. Ritzwoller (2011), Crust and uppermost mantle beneath the North China Craton, northeastern China, and the Sea of Japan from ambient noise tomography, *J. Geophys. Res.*, *116*, B12312, doi:10.1029/2011JB008637.

Zhou, L., J. Xie, W. Shen, Y. Zheng, Y. Yang, H. Shi, and M. H. Ritzwoller (2012), The structure of the crust and uppermost mantle beneath south China from ambient noise and earthquake tomography, *Geophys. J. Int.*, in press.

A. L. Levshin, M. H. Ritzwoller, and W. Shen, Center for Imaging the Earth's Interior, Department of Physics, University of Colorado Boulder, Boulder, CO 80309-0390, USA. (levshin@indurain.colorado.edu; michael. ritzwoller@colorado.edu; weisen.shen@colorado.edu)

Z. Xie and Y. Zheng, State Key Laboratory of Geodesy and Earth's Dynamics, Institute of Geodesy and Geophysics, Chinese Academy of Sciences, Wuhan 430077, China. (zujunxie@whigg.ac.cn; zhengyong@whigg. ac.cn)

Y. Yang, CCFS, GEMOC ARC National Key Centre, Department of Earth and Planetary Sciences, Macquarie University, Sydney, NSW 2109, Australia. (yingjie.yang@mq.edu.au)